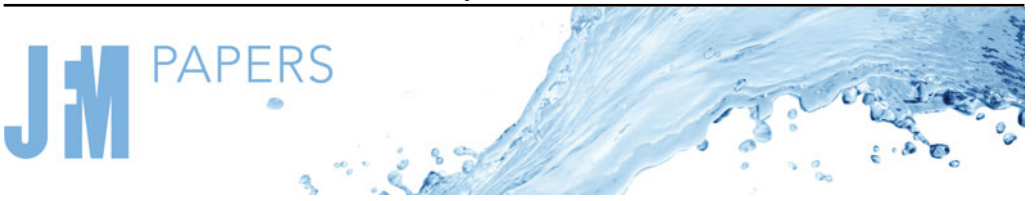
J. Fluid Mech. (2025), *vol.* 1018, A28, doi:10.1017/jfm.2025.10541



On the evolution of the mixing layer in rotation-driven Rayleigh–Taylor turbulence

Xin Xu[1], **Zhiye Zhao**[1,2], **Fenghui Lin**[1], **Pei Wang**[3], **Nan-Sheng Liu**[1] and **Xi-Yun Lu**[1]

[1]Department of Modern Mechanics, University of Science and Technology of China, Hefei, Anhui 230026, PR China

[2]Department of Mechanical and Aerospace Engineering, The Hong Kong University of Science and Technology, Clear Water Bay, Kowloon, Hong Kong

[3]National Key Laboratory of Computational Physics, Institute of Applied Physics and Computational Mathematics, Beijing 100094, PR China

Corresponding author: Zhiye Zhao, zzy12@ustc.edu.cn

(Received 14 August 2024; revised 27 July 2025; accepted 30 July 2025)

The evolution of the mixing layer in rotation-driven Rayleigh–Taylor (RT) turbulence is investigated theoretically and numerically. It is found that the evolution of the turbulent mixing layer in rotation-driven RT turbulence is self-similar, but the width of the mixing layer does not follow the classical quadratic growth observed in planar RT turbulence induced by constant external acceleration. Based on the approach used in cylindrical RT turbulence without rotation (Zhao *et al.* 2021, *Phys. Rev. E*, vol. 104, 055104), a theoretical model is established to predict the growth of mixing widths in rotation-driven RT turbulence, and the model's excellent agreement with direct numerical simulations (DNS) serves to validate its reliability. The model proposes a rescaled time that allows for the unification of the evolutions of the mixing layers in rotation-driven RT turbulence with various Atwood numbers and rotation numbers. It is further identified that the growth law described by the model of rotation-driven RT turbulence can be recovered to quadratic growth when the effects of geometrical curvature, radial inhomogeneity of the centrifugal force, and Coriolis force become negligible. Moreover, based on the DNS results, we find that turbulent mixing layers in rotation-driven RT turbulence cover a wide range of length scales. The strong rotation at the same Atwood number enhances the generation of fine-scale structures but is not conducive to overall fluid mixing within the mixing layer.

Key words: buoyancy-driven instability, rotating flows

https://doi.org/10.1017/jfm.2025.10541 Published online by Cambridge University Press

© The Author(s), 2025. Published by Cambridge University Press.

1. Introduction

Rayleigh–Taylor (RT) instability occurs at a perturbed interface between two fluids when an external acceleration points from the heavier to the lighter fluid (Rayleigh 1882; Taylor 1950). The RT instability and its induced RT turbulence are of great interest in various fields, including atmospheric physics (Caproni *et al.* 2015), deep ocean circulation (Cui & Street 2004), inertial confinement fusion (Bodner 1974), supernova explosion (Gelfand, Slane & Zhang 2009), aerosol transport (Hinds *et al.* 2002) and weather inversions (Schultz *et al.* 2006). The growth of the mixing layer is essential for understanding the fundamental characteristics of RT turbulence, making it important to study the evolution of the mixing layer in detail.

The evolution of the mixing layer in planar RT turbulence, induced by an external constant acceleration, has been extensively studied as it is the most fundamental model problem (Zhou 2017*a*,*b*). It is widely accepted that planar RT turbulence evolves towards self-similarity, with the mixing layer following the well-known quadratic growth, i.e. $h_i \sim \alpha_i A_t g t^2$. Here, $i = b, s$, h_b is the bubble mixing width, h_s is the spike mixing width, α_i is a dimensionless coefficient, the Atwood number is $A_t = (\rho_h - \rho_l)/(\rho_h + \rho_l)$, with ρ_h and ρ_l being the heavy and light fluid densities, respectively, and g is the constant external acceleration. This quadratic growth of mixing layer for planar RT turbulence was first described by Read (1984) and Youngs (1984). It was also obtained by Ristorcelli & Clark (2004) and Cook, Cabot & Miller (2004) using the similarity assumption and mass flux argument, respectively. Furthermore, as summarised by the review articles Zhou (2017*a*,*b*), the quadratic growth of mixing layer in planar RT turbulence has been supported by numerous experiments (Andrews & Spalding 1990; Dimonte 2000; Olson & Jacobs 2009; Akula *et al.* 2017) and simulations (Cherfils & Mikaelian 1996; Cook & Dimotakis 2001; Cabot & Cook 2006; Cabot & Zhou 2013; Zhao *et al.* 2020*a*).

Rotation-driven RT flow has garnered significant attention (Tao *et al.* 2013; Scase & Hill 2018; Huneault, Plant & Higgins 2019; Scase & Sengupta 2021) due to its occurrence on astrophysical scales with strong rotation (Scase & Sengupta 2021). In fact, rotation-driven flow has emerged as a popular flow configuration and has been extensively studied in recent years (Jiang *et al.* 2020, 2022; Ecke & Shishkina 2023; Zhong, Wang & Sun 2023; Yao *et al.* 2025). Moreover, a fundamental understanding of rotation-driven RT turbulence could potentially aid in further controlling inertial confinement fusion (Zhang *et al.* 2020) and magnetised target fusion (Buyko *et al.* 1997). Specifically, the rotation-driven RT system can be regarded as a limiting case of a rotating system in the absence of a gravitational field, with the instability occurring at the cylindrical interface between two concentric cylinders of fluid aligned on the axis of rotation. Based on the linear stability analysis conducted by Tao *et al.* (2013), it is observed that the perturbation of RT instability in a rotating system without external acceleration experiences exponential growth at the linear stage, with growth rate $\sqrt{\Omega^2 r_0 k A_t - A_t^2 \Omega^2}$, where Ω is the angular speed of the rotating system, k is the wavenumber, and r_0 is the initial position of the interface. Tao *et al.* (2013) demonstrated that the centrifugal effects described by the first term under the radical sign of the growth rate expression enhance the instability with heavy fluid inside the interface, while the Coriolis effect represented by the second term always diminishes the growth of instability. Later, Scase & Hill (2018) developed a new dispersion relation that takes into account the curvature of the interface, highlighting the influence of geometrical curvature on the growth of RT instability. Furthermore, experiments have demonstrated that the RT instability may be suppressed by rotating at a sufficient angular speed at the inner surface of an imploding liquid shell (Huneault *et al.* 2019). More recently, rotation-driven RT

https://doi.org/10.1017/jfm.2025.10541 Published online by Cambridge University Press

instability under three-dimensional (3-D) cylindrical geometry has been studied, where the initial perturbations exist in both axial and circumferential directions, and the linear growth rates in various cases are proposed (Scase & Sengupta 2021). Therefore, unlike planar RT systems induced by constant external acceleration, the rotation-driven RT system is governed by distinct physical mechanisms, including the effects of geometrical curvature, Coriolis force, and radial inhomogeneity of the centrifugal force.

Based on the above studies of rotation-driven RT instability, it is evident that the effects of geometrical curvature, the Coriolis force, and the radial inhomogeneity of the centrifugal force are also present in rotation-driven RT turbulence. Indeed, the evolution and flow features of the mixing layer in RT turbulence can be markedly influenced by each of these physical mechanisms. Specifically, considering the effect of geometrical curvature, Zhao *et al.* (2021) proposed that in cylindrical RT turbulence induced by a constant external radial acceleration, the outward mixing layer satisfies the hyperbolic cosine growth, and the inward mixing layer obeys the cosine growth, which are different from the quadratic growth of the mixing layer in planar geometry. Abarzhi & Sreenivasan (2022) revealed that the velocity scaling, velocity correlations, and spectra of specific kinetic energy in RT turbulence induced by space-varying acceleration differ significantly from those in RT turbulence induced by constant external acceleration. Furthermore, it is widely acknowledged that the Coriolis force imposes intriguing inhibitory effects on the growth of mixing layer in RT turbulence when the axis of system rotation is parallel to the direction of gravity, as evidenced by previous numerical studies (Carnevale *et al.* 2002; Boffetta, Mazzino & Musacchio 2016; Wei *et al.* 2022) and experimental results (Scase *et al.* 2017, 2020). The typical features of the mixing layer in RT turbulence have also been affected by the Coriolis force. For instance, the numerical simulation results indicate that the Coriolis force reduces the intensity of velocity fluctuations (Baldwin, Scase & Hill 2015; Boffetta *et al.* 2016), but enhances the fluid mixing in RT turbulence (Wei *et al.* 2022). In other forms of rotation-driven turbulence, such as centrifugal convection under supergravity (Teng *et al.* 2015; Jiang *et al.* 2020, 2022; Ecke & Shishkina 2023; Zhong *et al.* 2023; Yao *et al.* 2025), it has been shown that Coriolis forces induced by rotation can significantly influence flow structures and turbulent properties. The aforementioned observations indicate that the mixing layer evolution in rotation-driven RT turbulence, which is governed by the combined effects of geometrical curvature, Coriolis force, and the radial inhomogeneity of the centrifugal force (i.e. a radially varying inducing force), will experience a distinctive evolution compared to that in planar RT turbulence induced by an external constant acceleration and in cylindrical RT turbulence without rotation (Zhao *et al.* 2021). Investigating how to model the growth of the mixing layer affected by the Coriolis force, along with examining general flow features of RT turbulence, such as a wide range of length scales, self-similarity and mixed mass, are crucial in rotation-driven RT turbulence. To this end, this work explores the growth law and flow features of the mixing layer in rotation-driven RT turbulence.

In the present study, we numerically investigate the evolution of the mixing layer in rotation-driven RT turbulence with various rotational speeds and A_t. Following the approach used by Zhao *et al.* (2021) for modelling mixing layer growth in cylindrical RT turbulence without rotation, we have developed a model to describe mixing layer growth in rotation-driven RT turbulence. The remainder of this paper is organised as follows. The details of numerical simulation are described in § 2. The results and discussions, including the flow features and the theoretical model of the mixing layer, are reported in § 3. Finally, concluding remarks are addressed in § 4.

https://doi.org/10.1017/jfm.2025.10541 Published online by Cambridge University Press

2. Numerical simulations

2.1. *Governing equations and numerical method*

Given that compressible Navier–Stokes equations for Newtonian miscible fluids provide a more realistic portrayal of RT instabilities in high energy density physics and supernova explosions in astrophysics (Livescu 2013; Reckinger, Livescu & Vasilyev 2016; Gauthier 2017), they are employed to conduct direct numerical simulations (DNS) of rotation-driven RT turbulence. These equations are numerically solved in a cylindrical coordinate system (r, θ, z) to study the nonlinear evolution of the mixing layer in rotation-driven RT turbulence, as well as to examine the effects of rotational speed on the mixing layer. To this end, when non-dimensionalising the governing equations, we should ensure that the fluid properties are similar, and that the fluid density ratio and angular speed of rotational system can be adjusted. Therefore, we have chosen p_I^* and $\rho_I^* = (\rho_h^* + \rho_l^*)/2$ at the initial interface as the characteristic scales for pressure and density, respectively, where ρ_h^* and ρ_l^* are in sequence the heavy and light fluid densities. Then the characteristic velocity and temperature can be presented as $U_I^* = \sqrt{p_I^*/\rho_I^*}$ and $T_I^* = p_I^*(M_h^* + M_l^*)/(2\mathcal{R}^*\rho_I^*)$, respectively, with the perfect gas constant $\mathcal{R}^*$, and molar masses of heavy M_h^* and light M_l^* gases (Kord & Capecelatro 2019; Fu *et al.* 2022; Yuan *et al.* 2023). Note that the superscript $*$ denotes a dimensional physical quantity. The initial radius of the unperturbed interface r_0^* is used as the characteristic length scale. Thus the dimensionless Navier–Stokes equations in a reference frame rotating about the z axis read as

$$\frac{\partial \rho}{\partial t} + \boldsymbol{\nabla}\cdot(\rho \boldsymbol{u}) = 0, \tag{2.1}$$

$$\frac{\partial(\rho \boldsymbol{u})}{\partial t} + \boldsymbol{\nabla}\cdot(\rho \boldsymbol{u}\boldsymbol{u}) = -\boldsymbol{\nabla} p + \frac{1}{Re}\boldsymbol{\nabla}\cdot\boldsymbol{\sigma} - 2\,Ro\,\rho\,\boldsymbol{e}_z \times \boldsymbol{u} - Ro^2\,\rho\,\boldsymbol{e}_z \times (\boldsymbol{e}_z \times \boldsymbol{r}), \tag{2.2}$$

$$\frac{\partial(\rho e)}{\partial t} + \boldsymbol{\nabla}\cdot[(\rho e + p)\boldsymbol{u}] = \frac{1}{Re}\boldsymbol{\nabla}\cdot\left(\boldsymbol{\sigma}\cdot\boldsymbol{u} + \boldsymbol{q}^T + \boldsymbol{q}^Y\right) - Ro^2\,\rho[\boldsymbol{e}_z \times (\boldsymbol{e}_z \times \boldsymbol{r})]\cdot\boldsymbol{u}, \tag{2.3}$$

$$\frac{\partial(\rho Y_h)}{\partial t} + \boldsymbol{\nabla}\cdot(\rho Y_h \boldsymbol{u}) = \frac{1}{Re\,Sc}\boldsymbol{\nabla}\cdot(\rho D\,\boldsymbol{\nabla} Y_h). \tag{2.4}$$

Here, ρ is the density, p is pressure, $\boldsymbol{u} = (u_r, u_\theta, u_z)$ is the velocity, $\boldsymbol{e}_z$ is the unit vector along the z direction, $e = T/(\gamma - 1) + \boldsymbol{u}\cdot\boldsymbol{u}/2$ denotes the specific total energy with the temperature T and the ratio of specific heat $\gamma = 1.4$. Also, $Y_h = \rho_h/\rho$ is the mass fraction for heavy fluid, therefore the mass fraction for light fluid is $Y_l = 1 - Y_h$. The viscous stress tensor $\boldsymbol{\sigma}$ can be obtained by

$$\boldsymbol{\sigma} = 2\mu\boldsymbol{S} - \tfrac{2}{3}\mu\theta\boldsymbol{\delta}, \tag{2.5}$$

where the viscosity coefficient $\mu = (T)^{3/2}(1 + c)/(T + c)$ is calculated by the Sutherland law with $c = T_s^*/T_I^*$, where the Sutherland temperature is $T_s^* = 124$ K, and the characteristic temperature is $T_I^* = 273.15$ K. Here, 'K' represents the Kelvin scale of temperature; $\boldsymbol{S} = [\boldsymbol{\nabla}\boldsymbol{u} + (\boldsymbol{\nabla}\boldsymbol{u})^{\mathrm{T}}]/2$ is the strain-rate tensor, $\boldsymbol{\delta}$ is the unit tensor, and $\theta = \boldsymbol{\nabla}\cdot\boldsymbol{u}$ is the dilatation related to the compression/expansion motions of fluid parcels. The fluxes for the thermal $\boldsymbol{q}^T$ and interspecies mass $\boldsymbol{q}^Y$ diffusions are obtained by

$$\boldsymbol{q}^T = \frac{1}{Pr}\frac{\gamma\kappa}{\gamma - 1}\boldsymbol{\nabla} T, \quad \boldsymbol{q}^Y = \sum_{m=h,l}\frac{1}{Sc}C_{pm}T\rho D\,\boldsymbol{\nabla} Y_m, \tag{2.6}$$

respectively, where κ is the thermal conductivity, D is the diffusion coefficient, and C_{pm} is the constant-pressure specific heat. The fluid properties are defined as linear

https://doi.org/10.1017/jfm.2025.10541 Published online by Cambridge University Press

combinations of the individual species' properties weighted by the mass fractions, i.e. $f = \sum_{m=h,l} Y_m f_m$ (for $f = \mu, \kappa, D, C_p, C_v$). In addition, the dimensionless ideal gas equation of state $p = \rho T/M$ is adopted to close the governing equations, where the molar mass of fluid M is calculated by $1/M = Y_h/M_h + Y_l/M_l$.

The dimensionless parameters in governing equations (2.1)–(2.4) are Reynolds, Prandtl, Schmidt and rotation numbers, defined by

$$Re = \frac{\rho_I^* U_I^* r_0^*}{\mu_I^*}, \quad Pr = C_{pI}^* \frac{\mu_I^*}{\kappa_I^*}, \quad Sc = \frac{\mu_I^*}{D_I^* \rho_I^*}, \quad Ro = \frac{\Omega^* r_0^*}{U_I^*}, \tag{2.7}$$

respectively. Here, Re, Pr and Sc are related to the fluid properties and length scale of system. The value of Ro, as the sole dimensionless number related to the angular speed of the rotational system, determines the rotational speed when the fluid properties are similar (Zhu *et al.* 2022; Yang *et al.* 2023; Hu, Li & Yu 2024; Zhang & Wang 2024; Ceci & Pirozzoli 2025). In fact, the dimensionless angular speed can be formulated as $\Omega = \Omega^*/(U_I^*/r_0^*) = Ro$. Evidently, the rotation of the system increases as Ro increases.

In the present study, high-resolution numerical schemes have been employed to solve the governing equations (2.1)–(2.4). Specifically, the convection and diffusion terms are discretised by the seventh-order WENO scheme and the sixth-order central difference scheme, respectively. The temporal integration is performed by the standard third-order Runge–Kutta method. Overall, our numerical approach is highly reliable in simulating RT turbulence, as demonstrated by our previous studies over a broad range of RT flow regimes (Zhao *et al.* 2020*b*, 2021; Fu *et al.* 2022).

2.2. *Flow field initialisation*

The rotation-driven RT turbulence arises within a rotating cylindrical system consisting of an inner fluid with heavy density ρ_h and an outer fluid with light density ρ_l as depicted in figure 1. The flow fields are initialised as follows. To avoid the effect of background stratification on the evolution of RT turbulence, the density field is initialised as uniform, such that $\rho_h = 1 + A_t$ for the inner fluid, and $\rho_l = 1 - A_t$ for the outer fluid (Scase & Hill 2018). Here, the Atwood number A_t is defined as

$$A_t = \frac{\rho_h - \rho_l}{\rho_h + \rho_l}. \tag{2.8}$$

Moreover, the initial velocity field is set to be zero. According to the hydrostatic equilibrium,

$$\frac{\partial p}{\partial r} = \begin{cases} -Ro^2(1 + A_t)r, & r < r_0, \\ -Ro^2(1 - A_t)r, & r > r_0, \end{cases} \tag{2.9}$$

the initial pressure can be determined by assuming $p = 1$ at the interface. Additionally, to avoid strong discontinuities in the initial field, a very thin mixing layer is initially set up. This initialisation approach is widely employed in RT flow simulation (Gauthier 2017; Luo & Wang 2021), and the density distribution can be expressed as

$$\rho(r) = (1 + A_t)\, H^-((r - r_0)/\delta) + (1 - A_t)\, H^+((r - r_0)/\delta), \tag{2.10}$$

where $H^+(x) = (1 + \mathrm{erf}(x))/2$, $H^-(x) = (1 - \mathrm{erf}(x))/2$, $\mathrm{erf}(x)$ is the error function, and δ is the thickness of the initial mixing layer. For the present simulations, δ is set to $\delta = 10\Delta_r$, where Δ_r is the width of the radial grid.

To attain fully developed rotation-driven RT turbulence, the interface at $r_0 = 1$ is perturbed using a multi-mode perturbation, given by $r(\theta) = r_0 + \sum_{n_\theta} A_m \cos(n_\theta \theta + \phi_\theta)$ for

https://doi.org/10.1017/jfm.2025.10541 Published online by Cambridge University Press

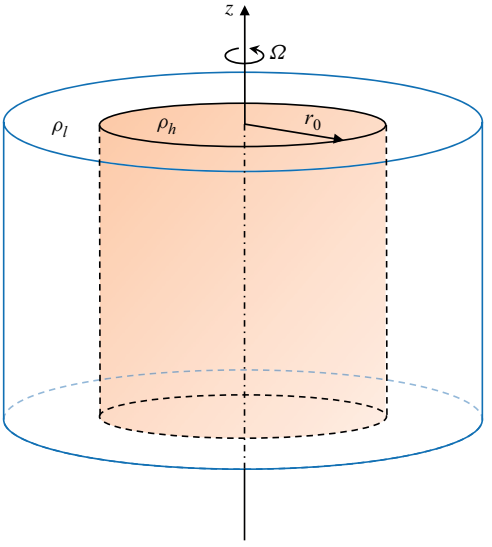


Figure 1. A schematic of the cylindrical flow domain. The system is rotating with angular speed Ω, and the fluid densities in the inner (heavy) and outer (light) layers are denoted by ρ_h and ρ_l, respectively.

two-dimensional (2-D) cases, and $r(\theta, z) = r_0 + \sum_{n_\theta, n_z} A_m \cos(n_\theta \theta + \phi_\theta) \cos(2\pi n_z z / L_z + \psi_z)$ for 3-D cases. Here, $L_z = 2\pi$ is the axial length. The numbers of perturbation waves in the circumferential (n_θ) and axial (n_z) directions are chosen within the ranges $30 \leqslant n_\theta \leqslant 60$ for 2-D cases and $30 \leqslant \sqrt{n_\theta^2 + n_z^2} \leqslant 60$ for 3-D cases. Here, ϕ_θ and ψ_z are random phases in the circumferential and axial directions, respectively. According to a previous study (Zhao *et al.* 2021), the perturbation amplitude is set as $A_m = 10^{-3}$ for the 2-D cases and $A_m = 3 \times 10^{-4}$ for the 3-D cases. Here, the value of A_m in the 3-D cases is smaller than that in the 2-D cases. This is due to the greater number of superimposed perturbed modes in the 3-D cases compared to the 2-D cases. In this way, the root mean squares of the initial perturbations in both 2-D and 3-D cases are of the same order, $O(10^{-3})$, with a narrow range from 2.4×10^{-3} to 3.2×10^{-3} in the present simulations.

To verify our proposed model for mixing layer and flow features of rotation-driven RT turbulence, this study selects a wide range of A_t values from 0.1 to 0.9, and of Ro values from 0.25 to 2.0. Here, A_t and Ro jointly determine the driving force of the RT system, and are typically the focus of the RT community (Zhou, Cabot & Thornber 2016; Gauthier 2017; Zhou 2017*b*; Livescu, Wei & Brady 2021; Abarzhi & Sreenivasan 2022; Fu *et al.* 2022, 2023; Suchandra & Ranjan 2023). Moreover, the Prandtl, Schmidt and Reynolds numbers in the governing equations are fixed at $Pr = 0.72$, $Sc = 1$ and $Re = 40\,000$, respectively, to ensure that the fluid properties are similar for present simulations. The detailed parameter set is given in table 1. Moreover, to avoid a pole singularity at the centre of cylindrical coordinates, a micro-hole with radius $r_{min} = 0.05$ is dug out. Previous studies have shown that the impact of this strategy on the evolution of RT flow can be ignored (Zhao *et al.* 2021). Furthermore, we performed DNS in a circular domain $D = \{(r, \theta) \mid r_{min} \leqslant r \leqslant r_{max},\ 0 \leqslant \theta < 2\pi\}$ for 2-D cases, and in a cylindrical domain $D = \{(r, \theta, z) \mid r_{min} \leqslant r \leqslant r_{max},\ 0 \leqslant \theta < 2\pi,\ 0 \leqslant z \leqslant 2\pi\}$ for 3-D cases, where $r_{max} = 2.5 r_0$. Following previous work (Wang *et al.* 2013; Guo *et al.* 2014; Liu *et al.* 2014; Zhao *et al.* 2021), the velocity, density, temperature and species mass fractions in the inner

https://doi.org/10.1017/jfm.2025.10541 Published online by Cambridge University Press

Case	Dimension	A_t	Ro	Re	Pr	Sc	M	N	P
A01R025	2-D	0.1	0.25	40 000	0.72	1	1200	1600	—
A01R10	2-D	0.1	1.0	40 000	0.72	1	1200	1600	—
A01R20	2-D	0.1	2.0	40 000	0.72	1	1200	1600	—
A05R025	2-D	0.5	0.25	40 000	0.72	1	1200	1600	—
A05R10	2-D	0.5	1.0	40 000	0.72	1	1200	1600	—
A05R20	2-D	0.5	2.0	40 000	0.72	1	1200	1600	—
A09R025	2-D	0.9	0.25	40 000	0.72	1	1200	1600	—
A09R10	2-D	0.9	1.0	40 000	0.72	1	1200	1600	—
A09R20	2-D	0.9	2.0	40 000	0.72	1	1200	1600	—
3DA01R025	3-D	0.1	0.25	40 000	0.72	1	600	800	800
3DA01R20	3-D	0.1	2.0	40 000	0.72	1	600	800	800
3DA05R025	3-D	0.5	0.25	40 000	0.72	1	600	800	800
3DA05R20	3-D	0.5	2.0	40 000	0.72	1	600	800	800
3DA09R025	3-D	0.9	0.25	40 000	0.72	1	600	800	800
3DA09R20	3-D	0.9	2.0	40 000	0.72	1	600	800	800

Table 1. Simulation parameters for DNS. Here, M, N and P represent the numbers of grid points in the radial, circumferential and axial directions, respectively.

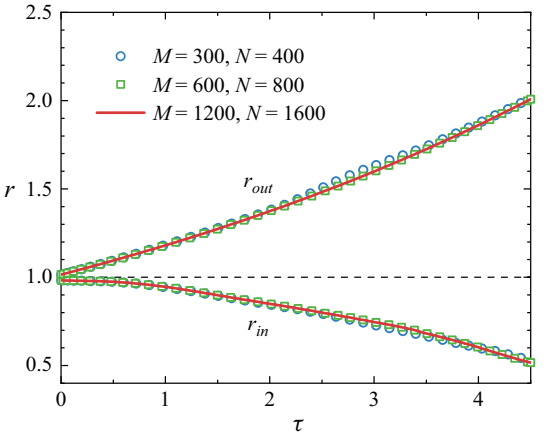


Figure 2. The positions of outer and inner frontiers of the mixing layer as functions of τ for the case A09R20 with three different grid resolutions.

cylinder at $r = r_{min}$ and the outer cylinder at $r = r_{max}$ are fixed at their initial values to ensure hydrostatic equilibrium. Additionally, the periodic boundary conditions are applied in the circumferential direction, and in the axial direction for the 3-D cases.

To ensure the accuracy of the simulation results in predicting the evolution of the rotation-driven RT turbulent mixing layer, a grid convergence study is carried out for the case A09R20. Specifically, three different grid sizes are tested. The radial direction is discretised with $M = 300$, 600 and 1200 uniform grid points, while the circumferential direction corresponds to $N = 400$, 800 and 1600 uniform grid points, respectively. Figure 2 illustrates the positions of outer r_{out} and inner r_{in} frontiers of the mixing layer as functions of the rescaled time $\tau = A_t(e^{-2\Omega t} + 2\Omega t - 1)$, where the angular speed of reference frame is $\Omega = Ro$ for the present simulations. This rescaled time can be used to describe the evolution of the mixing layer in rotation-driven RT turbulence with various density ratios and angular speeds of the rotating system, and its determination is given by the

https://doi.org/10.1017/jfm.2025.10541 Published online by Cambridge University Press

Case	Re_H	Re_λ	$\min(\eta/\Delta_\theta)$	η/Δ_r	η/Δ_z	$[\lvert F_{cor}\rvert]$	$[\lvert F_{cen}\rvert]$
A01R025	11 000	108	6.54	31.45	—	0.02	0.06
A01R10	28 000	175	4.24	20.39	—	0.13	0.95
A01R20	38 000	204	3.26	15.68	—	0.38	3.76
A05R025	14 000	119	5.94	28.56	—	0.02	0.05
A05R10	37 000	192	3.30	15.87	—	0.25	0.83
A05R20	54 000	232	2.86	13.75	—	0.70	3.33
A09R025	21 000	146	4.82	23.18	—	0.06	0.05
A09R10	47 000	212	2.96	14.23	—	0.55	0.75
A09R20	71 000	268	2.66	12.79	—	1.74	3.00
3DA01R025	11 000	113	2.54	12.21	4.89	0.02	0.06
3DA01R20	39 000	208	1.31	6.30	2.52	0.37	3.72
3DA05R025	13 000	112	2.10	10.10	4.04	0.03	0.05
3DA05R20	55 000	238	1.11	5.34	2.14	0.72	3.28
3DA09R025	21 000	148	1.77	8.51	3.40	0.06	0.05
3DA09R20	72 000	277	1.01	4.86	1.94	1.80	3.00

Table 2. Statistics for DNS at the end of simulations, namely, the rescaled time $\tau = 4.5$. Here, Δ_r, Δ_θ and Δ_z represent the grid widths in the radial, circumferential and axial directions, respectively.

establishment of a theoretical model predicting the growth of the mixing layer in the next section. As depicted in figure 2, the time series of r_{out} and r_{in} for the two finer grids collapse together. Here, r_{out} and r_{in} can be determined based on the widths of the inward mixing layer h_{in} and the outward mixing layer h_{out}, i.e. $r_{out} = r_0 + h_{out}$ and $r_{in} = r_0 - h_{in}$. Here, h_{in} and h_{out} are calculated by

$$h_{in} = 4\int_{r_{min}}^{r_0} \langle X_h\rangle\,(1-\langle X_h\rangle)\,\mathrm{d}r \tag{2.11}$$

and

$$h_{out} = 4\int_{r_0}^{r_{max}} \langle X_h\rangle\,(1-\langle X_h\rangle)\,\mathrm{d}r, \tag{2.12}$$

respectively. Here, $\langle\,\rangle$ represents the spatial average over the θ–z plane, and the mole fraction of the heavy fluid is defined as $X_h = (\rho-\rho_l)/(\rho_h-\rho_l)$. In addition, the width of the mixing layer can be defined as $h = h_{in} + h_{out}$. Hence it is evident that the grid resolution corresponding to $M \times N = 600 \times 800$ is adequate for analysing the evolution of turbulent mixing layer. To this end, the 2-D cases utilise the grid resolution $M \times N = 1200 \times 1600$. On the other hand, the 3-D cases employ the grid resolution $M \times N \times P = 600 \times 800 \times 800$. The grid resolutions are listed in table 1.

To further demonstrate that the resolution of the present grid is adequate for analysing RT turbulence, the ratios of the Kolmogorov length scale to the grid widths are examined. Since both the radial and axial grids are uniform, the widths are given by $\Delta_r = 2.45r_0/M$ and $\Delta_z = 2\pi r_0/P$, respectively. The width of the circumferential grid increases with increasing r, reaching a maximum $\max(\Delta_\theta) = 5\pi r_0/N$ at $r = 2.5r_0$. The Kolmogorov length scale η is defined as

$$\eta = \frac{1}{\sqrt{Re}}\frac{1}{\sqrt{[\rho]}}\left(\frac{[\mu]^3}{[\varepsilon]}\right)^{1/4}. \tag{2.13}$$

Here, [ ] represents the spatial average over the mixing layer. As shown in table 2, it is confirmed that $\min(\eta/\Delta_\theta)$, η/Δ_r, $\eta/\Delta_z \geqslant 1.0$ at the end of all simulations. This indicates

https://doi.org/10.1017/jfm.2025.10541 Published online by Cambridge University Press

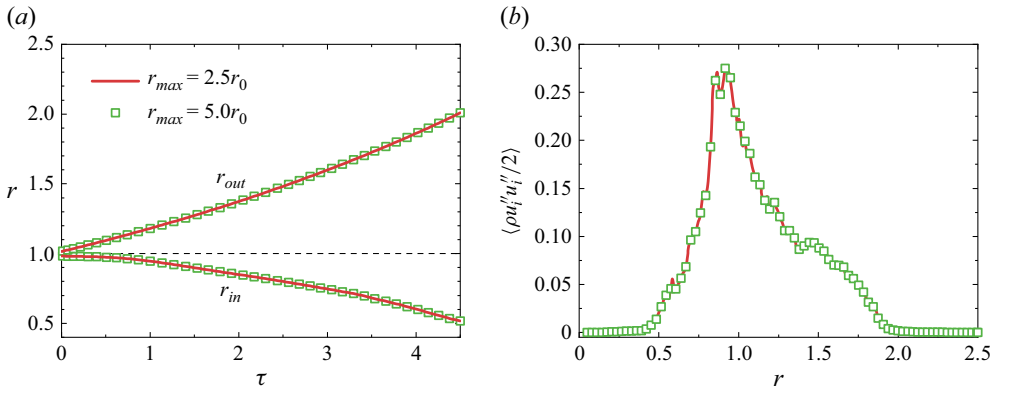


Figure 3. (*a*) The positions of the outer and inner frontiers of the mixing layer as functions of τ. (*b*) The radial distributions of the turbulent kinetic energy at $\tau = 4.5$ for the case A09R20 with different computational domains.

that the resolution of the present grid is adequate for analysing RT turbulence (Yeung & Pope 1989; Zhao, Betti & Aluie 2022).

To demonstrate that the computational boundary $r_{max} = 2.5r_0$ is enough in the current simulations, the typical case A09R20, which achieves the highest Re_H value at the end of simulation, is simulated using a larger boundary $r_{max} = 5.0r_0$. The comparisons of key statistics between these two different computational boundary sizes are presented in figure 3. It is evident that the positions of the mixing frontiers with different values of r_{max} collapse together during the evolution of the mixing layer. Furthermore, the radial distributions of turbulent kinetic energy $\langle \rho u_i'' u_i'' / 2 \rangle$ also collapse well, indicating that there are no potential-flow modes artificially pinned down to zero by the boundary $r_{max} = 2.5r_0$. Here, the velocity fluctuation based on the Favre average is given by $u_i'' = u_i - \langle \rho u_i \rangle / \langle \rho \rangle$. The two comparisons above show that $r_{max} = 2.5r_0$ is indeed sufficient for the current simulations.

Furthermore, the outer-scale Reynolds number Re_H, and Taylor micro-scale Reynolds number Re_λ, at the end of the simulation are calculated and listed in table 2 to confirm that the RT flow has reached a turbulent state. Here, Re_H and Re_λ are defined as

$$Re_H = \frac{\rho_I^* H^* \dot{H}^*}{\mu_I^*} = Re H \dot{H}, \quad Re_\lambda = Re \frac{[\rho]\, \lambda \sqrt{[u_i u_i]}}{\sqrt{3}\, [\mu]}, \tag{2.14}$$

respectively, where H denotes the visual width of the mixing region, defined as the difference of radial locations at $\langle Y_h \rangle = 0.01$ and $\langle Y_h \rangle = 0.99$. The Taylor micro-scale λ is defined as

$$\lambda = \sqrt{\frac{[u_i u_i]}{[(\partial u_r/\partial r)^2 + ((1/r)\, \partial u_\theta/\partial \theta)^2 + (\partial u_z/\partial z)^2]}}. \tag{2.15}$$

As A_t and Ro increase, both Re_H and Re_λ increase significantly. The values of Re_H reach the order of 10^4 for all cases, and Re_λ ranges from 100 to 300. According to Dimotakis (2000), fully-developed turbulent flow requires an outer-scale Reynolds number $Re_H \gtrsim 10^4$, or a Taylor Reynolds number $Re_\lambda \gtrsim 100$. Hence the simulated flows have indeed achieved a turbulent state (Cook & Dimotakis 2001; Zhou 2013; Tritschler *et al.* 2014). Additionally, the Re_H value of the present simulation is indeed smaller than the Re_H value observed in astrophysical phenomena (e.g. in type-Ia supernovae, $Re_H \sim 10^{14}$; Woosley, Wunsch & Kuhlen 2004). However, the following discussions regarding the evolution of

https://doi.org/10.1017/jfm.2025.10541 Published online by Cambridge University Press

the mixing layer and the fluid mixing characteristics are valuable for understanding flow in astrophysical phenomena. This is because the growth rate and mixing rate of RT turbulence show weak dependencies on Reynolds number for $Re_H > 10^4$, as indicated in the study by Cabot & Cook (2006).

Additionally, the average magnitudes of the Coriolis force $[|F_{cor}|]$ and centrifugal force $[|F_{cen}|]$ within the mixing layer at the end of the simulations are presented in table 2 to evaluate the significance of these forces in rotation-driven RT turbulence. Here, $F_{cor} = -2\,Ro\,\rho\,\boldsymbol{e}_z \times \boldsymbol{u}$ and $F_{cen} = Ro^2 \rho r\,\boldsymbol{e}_r$. According to these expressions, it is clear that the centrifugal force varies spatially, and the Coriolis force is related to the flow velocity. As shown in table 2, it is evident that $[|F_{cor}|]$ remains of the same value order as $[|F_{cen}|]$ in all cases, indicating that the Coriolis force is significant and must be considered when establishing the model for the growth of the mixing layer.

3. Results and discussions

The flow features for rotation-driven RT turbulent mixing layer, such as a wide range of length scales, self-similarity, mixing width and mixed mass, are examined by means of DNS in this section. Moreover, a theoretical model is proposed to predict the growth of the mixing width in the rotation-driven RT turbulence.

3.1. *Wide range of length scales in the turbulent mixing layer*

Figures 4 and 5 display snapshots of the instantaneous mass fraction fields for all 2-D cases, and isosurfaces of the mass fraction for 3-D cases, respectively, at the end of the simulation when the rescaled time is $\tau = 4.5$. Evidently, the mixing layer for all cases exhibits fine-scale structures and large patches. Specifically, the formation of large-scale structures in the turbulent mixing layer is attributed to the merging of bubbles and spikes. The fine-scale structures are continuously generated along the evolutionary interface between heavy and light fluids (Gauthier 2017). It is noteworthy that the cases with high A_t and Ro (e.g. case A09R20) exhibit more fine-scale structures compared to the cases with low A_t and Ro (e.g. case A01R025). This is due to the fact that a higher Re_H is achieved for the case with higher A_t and Ro at the same rescaled time. The visualisations clearly demonstrate the wide range of length scales present in rotation-driven RT turbulence.

To quantitatively describe the wide range of length scales in rotation-driven RT turbulence, the density spectra defined by (Tritschler *et al.* 2014; Ge *et al.* 2020)

$$E_\rho(r, k_\theta, t) = \frac{\widehat{\rho'}^{*}\,\widehat{\rho'}(r, k_\theta, t)}{\Delta k_\theta}. \tag{3.1}$$

are examined. Here, k_θ is the wavenumber in the circumferential direction, and the spectra bin size is given by $\Delta k_\theta = \Delta n\, 2\pi/(2\pi r_0) = 1$, with $\Delta n = 1$ at the location of the initial interface ($r_0 = 1$). In addition, $\widehat{\rho'}$ is the Fourier transformation of the density fluctuation, and $\widehat{\rho'}^{*}$ is its complex conjugate. All the density spectra shown in figure 6 are calculated at the interface $r_0 = 1$ and normalised by total spectral density $E_{tot} = \int E_\rho \,\mathrm{d}k_\theta$. For 2-D cases, $k_{\theta,max} = 800$ with $N = 1600$ circumferential grid points; here, $k_{\theta,max}$ is maximum wavenumber. In contrast, for 3-D cases, $k_{\theta,max} = 400$ with $N = 800$ circumferential grid points. Moreover, the density spectra for 3-D cases are averaged in the axial direction. To reveal the influence of rotational speed on the flow structures in rotation-driven RT turbulence, we compare the spectra with the same A_t, and meanwhile those spectra are evaluated at the moment when Re_H reaches a same value. Specifically, the Re_H values in figure 6(*a*,*d*) ($A_t = 0.1$), figure 6(*b*,*e*) ($A_t = 0.5$) and figure 6(*c*,*f*) ($A_t = 0.9$) are 11 000,

https://doi.org/10.1017/jfm.2025.10541 Published online by Cambridge University Press

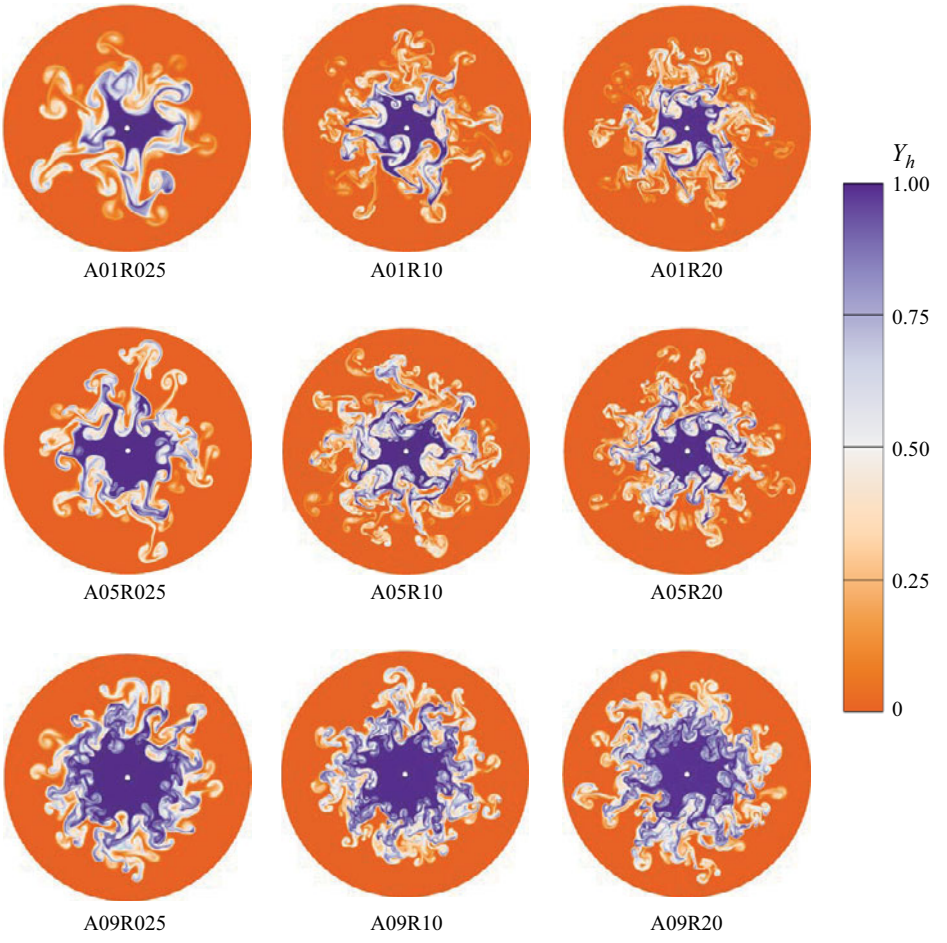


Figure 4. Snapshots of instantaneous fields for the mass fraction of heavy fluid for 2-D cases at the rescaled time $\tau = 4.5$. Here, the radii of all panels are $2.5r_0$.

14 000 and 21 000, respectively. Notably, the widths of mixing layers h for all cases at the moment shown in figure 6 are approximately of the order of r_0. Evidently, the rotation-driven RT flows cover a wide range of length scales, including the scales for initial perturbations shaded in orange, as well as other scales excited by the nonlinear interaction of bubbles and spikes. This demonstrates that a turbulent state is achieved when Re_H reaches the order of 10^4 (Cook & Zhou 2002). Interestingly, at the same A_t and Re_H, the energy spectra for $Ro = 0.25$ are smaller than those for $Ro = 1.0$ and $Ro = 2.0$ in the 2-D cases within the high wavenumber range, as indicated by the blue shading. Similarly, the spectra for $Ro = 0.25$ are also smaller than those for $Ro = 2.0$ in the 3-D cases with the high wavenumber range at the same A_t and Re_H. This finding suggests that strong rotation at the same A_t promotes the generation of small-scale structures in rotation-driven RT turbulence. Moreover, for 2-D cases with the same A_t, the spectra for $Ro = 1.0$ and 2.0 are nearly identical. This observation is related to the dynamics of the flow. Specifically, as shown in table 3, at the same A_t, the ratios of average magnitude of Coriolis force to that of centrifugal force at $r = 1$ are nearly similar for the 2-D cases $Ro = 1.0$ and 2.0. The ratios for $Ro = 1.0$ and 2.0 are significantly smaller than the ratio for $Ro = 0.25$. The above phenomena indicate that at the same A_t and Re_H, the nearly identical spectra for $Ro = 1.0$

https://doi.org/10.1017/jfm.2025.10541 Published online by Cambridge University Press

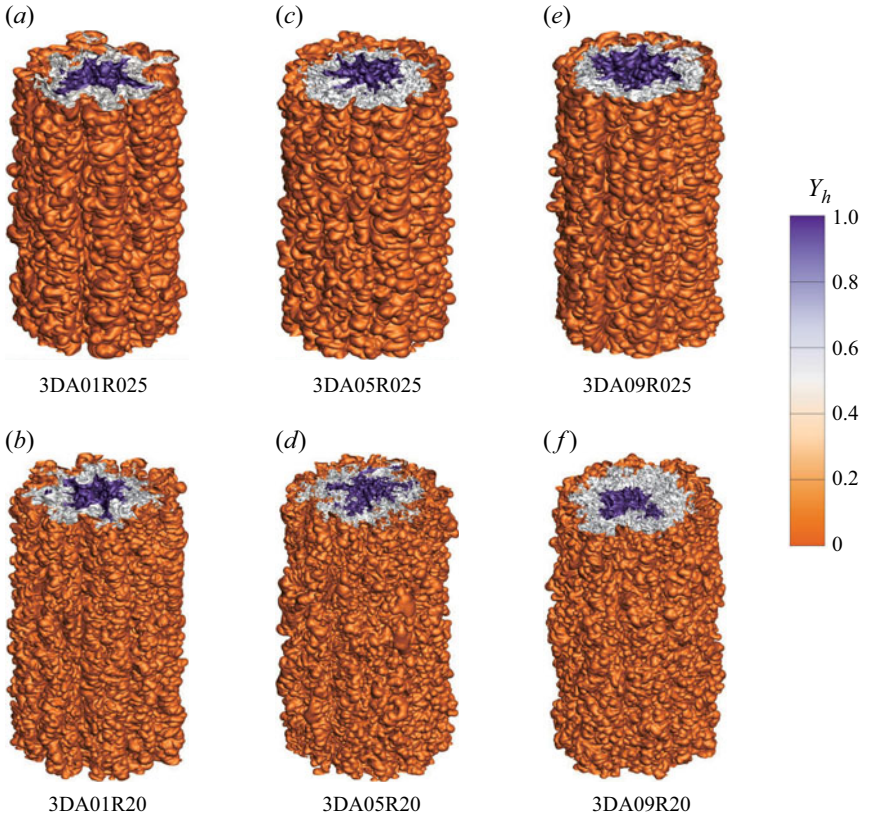


Figure 5. Isosurfaces of the mass fraction of heavy fluid (orange for $Y_h = 0.01$, grey for $Y_h = 0.5$, and purple for $Y_h = 0.99$) for 3-D cases at the rescaled time $\tau = 4.5$.

and 2.0 correspond to similar ratios, while a larger ratio in the case $Ro = 0.25$ corresponds to a reduction in the spectrum. It is important to note that the correlation between the spectral features and the ratios of forces is merely an interesting phenomenon. The physical mechanisms underlying these spectral features require further in-depth investigation.

To further confirm the beneficial effect of rotation on the generation of small-scale structures, the ratio of total turbulent kinetic energy (E_t) of mixing layer, representing the small-scale intensity in mixing layer, to total kinetic energy (E_k) is examined. Here, $E_t = (1/2)\int_V \rho u_i'' u_i'' \,\mathrm{d}V$ with velocity fluctuation u_i'', and $E_k = (1/2)\int_V \rho u_i u_i \,\mathrm{d}V$, where the integration domain V corresponds to the mixing layer. Figure 7 presents the temporal evolution of the ratio of E_t to E_k for 2-D and 3-D cases. Clearly, E_t/E_k increases as Ro increases under the same values of A_t, providing further evidence that strong rotation promotes the generation of small-scale structures in rotation-driven RT turbulence.

3.2. *Self-similarity feature of the turbulent mixing layer*

Another important flow feature of RT turbulence is self-similarity, which can be observed from the distribution of mean mass fraction across the mixing layer (Livescu *et al.* 2021; Abarzhi & Sreenivasan 2022). To confirm whether the rotation-driven RT turbulence exhibits the self-similarity, four typical cases, namely A01R025, A09R20, 3DA01R025 and 3DA09R20, are examined. These four cases are selected as they achieve the lowest

https://doi.org/10.1017/jfm.2025.10541 Published online by Cambridge University Press

Case	$\langle\lvert F_{cor}\rvert\rangle/\langle\lvert F_{cen}\rvert\rangle$
A01R025	0.38
A01R10	0.24
A01R20	0.23
A05R025	0.41
A05R10	0.29
A05R20	0.27
A09R025	0.57
A09R10	0.39
A09R20	0.36

Table 3. The ratio of the average magnitude of the Coriolis force $\langle|F_{cor}|\rangle$ to that of centrifugal force $\langle|F_{cen}|\rangle$ on the interface $r_0 = 1$ at the time corresponding to figure 6, for the 2-D cases.

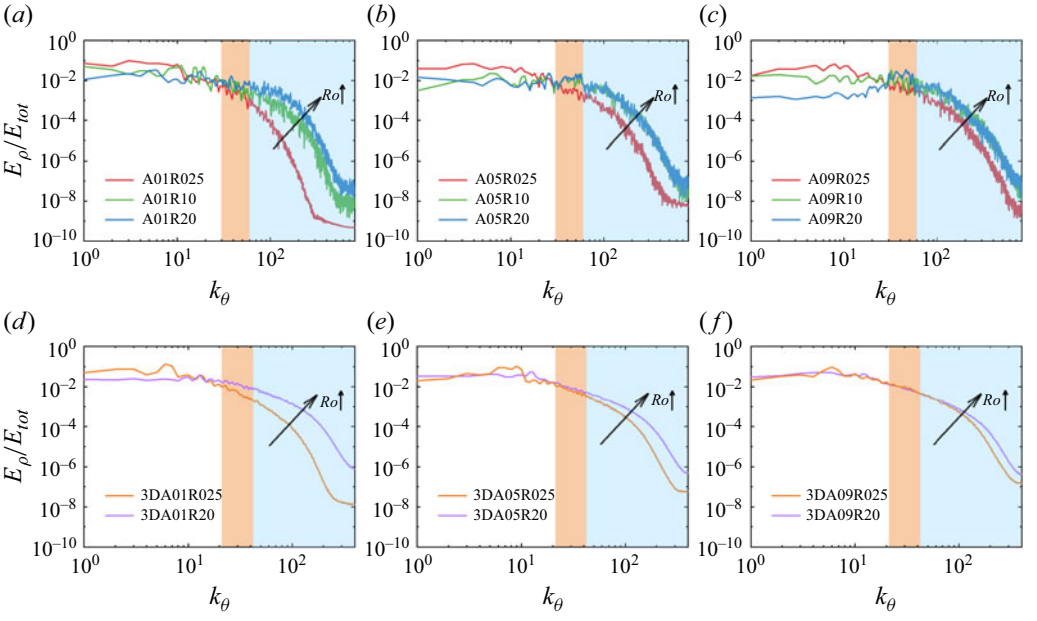


Figure 6. The density energy spectra at $r = 1$ in the circumferential direction, with (a,d) $A_t = 0.1$, $Re_H = 11\,000$, (b,e) $A_t = 0.5$, $Re_H = 14\,000$, and (c,f) $A_t = 0.9$, $Re_H = 21\,000$. The wavenumbers of initial perturbations are shaded in orange, and the wavenumbers corresponding to the small scales affected by the rotation are shaded in blue. The black arrows in each panel indicate an increase in Ro, corresponding to an increase in rotation.

or highest values of Re_H at the end of the 2-D and 3-D simulations, respectively. Figure 8 presents the radial distributions of the mean mass fraction of the heavy fluid at four different moments for these cases. As time progresses, the decrease of mass fraction along the radial direction becomes more gradual, indicating an increasing mixing width. Nevertheless, the distribution of mass fraction of heavy fluid exhibits a similar radial decreasing trend for each case, suggesting the self-similarity in rotation-driven RT turbulence. Therefore, the distribution of mean mass friction of heavy fluid can be represented as (Ristorcelli & Clark 2004)

https://doi.org/10.1017/jfm.2025.10541 Published online by Cambridge University Press

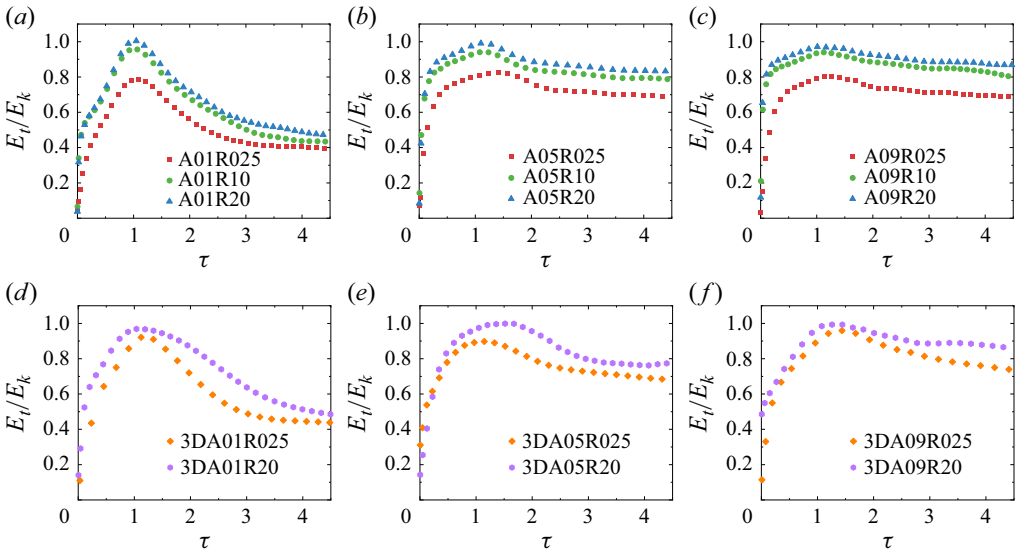


Figure 7. Temporal evolution of ratios of the turbulent kinetic energy to the total kinetic energy for 2-D cases with (*a*) $A_t = 0.1$, (*b*) $A_t = 0.5$, (*c*) $A_t = 0.9$, and 3-D cases with (*d*) $A_t = 0.1$, (*e*) $A_t = 0.5$, (*f*) $A_t = 0.9$.

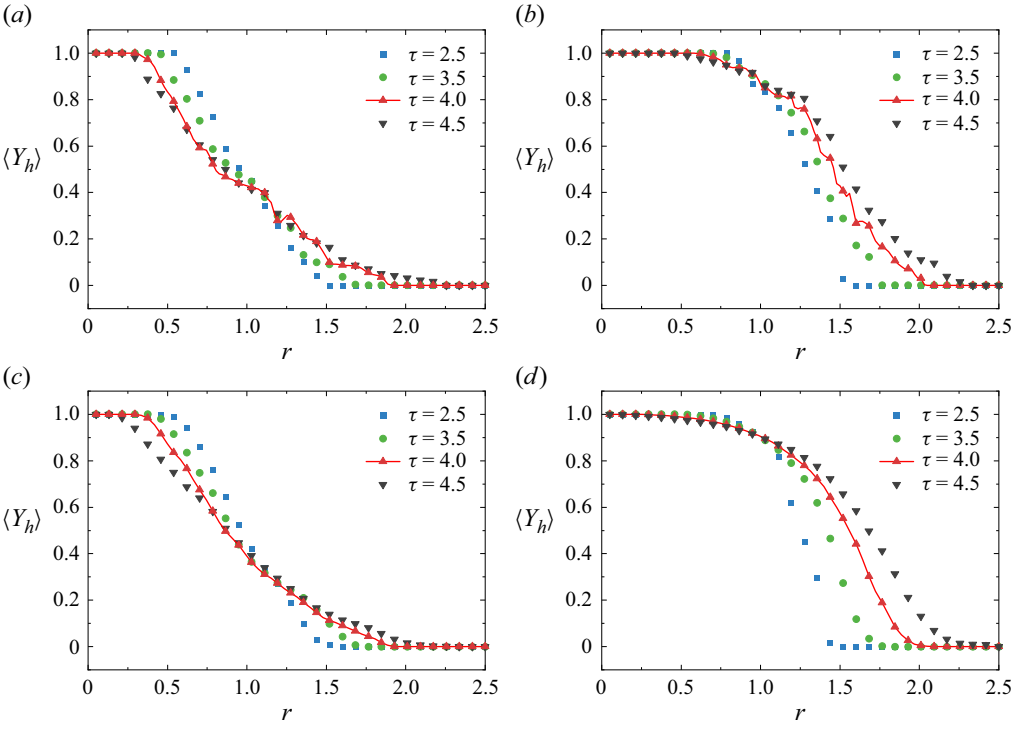


Figure 8. The radial distributions of mean mass fraction of heavy fluid at four different moments for cases (*a*) A01R025, (*b*) A09R20, (*c*) 3DA01R025 and (*d*) 3DA01R20. For clarity in the presentation, the solid line $\tau = 4.0$ is plotted.

https://doi.org/10.1017/jfm.2025.10541 Published online by Cambridge University Press

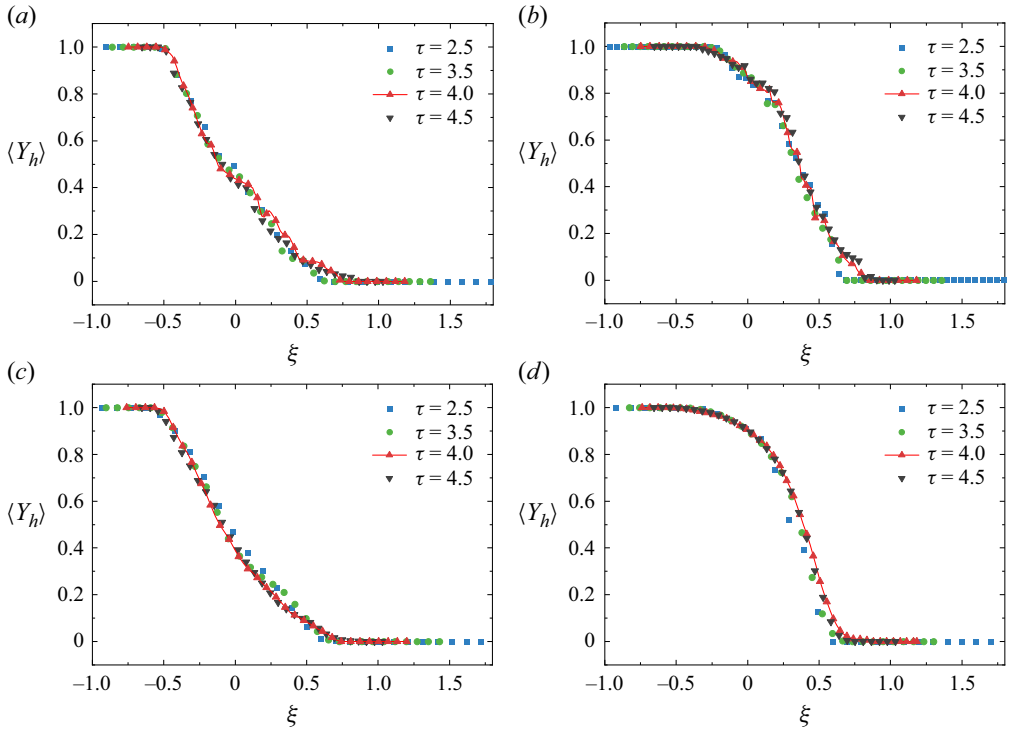


Figure 9. The distributions of mean mass fraction of heavy fluid at four different moments versus similarity variable ξ for cases (*a*) A01R025, (*b*) A09R20, (*c*) 3DA01R025 and (*d*) 3DA01R20.

$$\langle Y_h \rangle(r, t) = Y_0 \, F_Y(\xi), \quad \xi = \frac{r - r_0}{h(t)}, \tag{3.2}$$

where Y_0 is the scaling coefficient, $F_Y(\xi)$ is the spatial similarity function, and the mixing width h is defined as the sum of widths of the inward and outward mixing layers, i.e. $h = h_{in} + h_{out}$.

As shown in figure 9, the distributions of mean mass fraction at different moment instances collapse nearly onto a single curve for these representative cases. This suggests that the rotation-driven RT flow achieves a turbulent state with self-similarity (Youngs 2013; Hillier 2020). Additionally, it is worth noting that the growth law $h(t)$ of the mixing width, as shown in (3.2), is of critical importance in the self-similarity of RT turbulence.

3.3. *Width and mixed mass of the turbulent mixing layer*

The width of the mixing layer h is a critical measurement in RT turbulence, thus the temporal evolution of the mixing width in rotation-driven RT turbulence is examined and shown in figure 10. Evidently, the mixing layer growth in rotation-driven RT turbulence does not scale as t^2 at late time, which is dramatically different from the planar RT turbulence induced by constant external acceleration g (Cook *et al.* 2004; Ristorcelli & Clark 2004; Zhao *et al.* 2020*a*). This indicates that the model of planar RT turbulence, which includes only buoyancy effects, is insufficient for predicting the growth of the mixing width in the present simulations where the Coriolis force is significant. Thus it is essential to develop a new theoretical model to predict the growth of the mixing width

https://doi.org/10.1017/jfm.2025.10541 Published online by Cambridge University Press

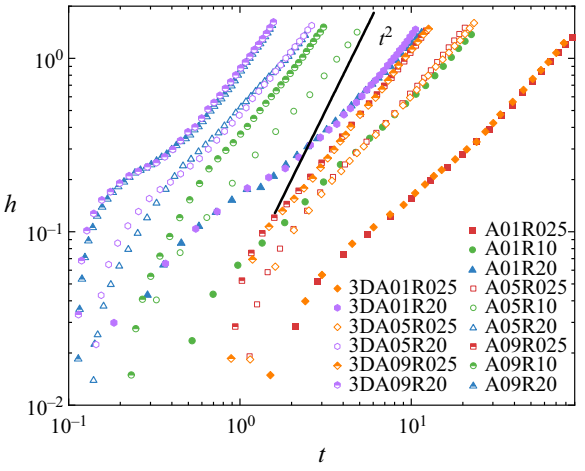


Figure 10. Temporal evolutions of the width of the mixing layer h.

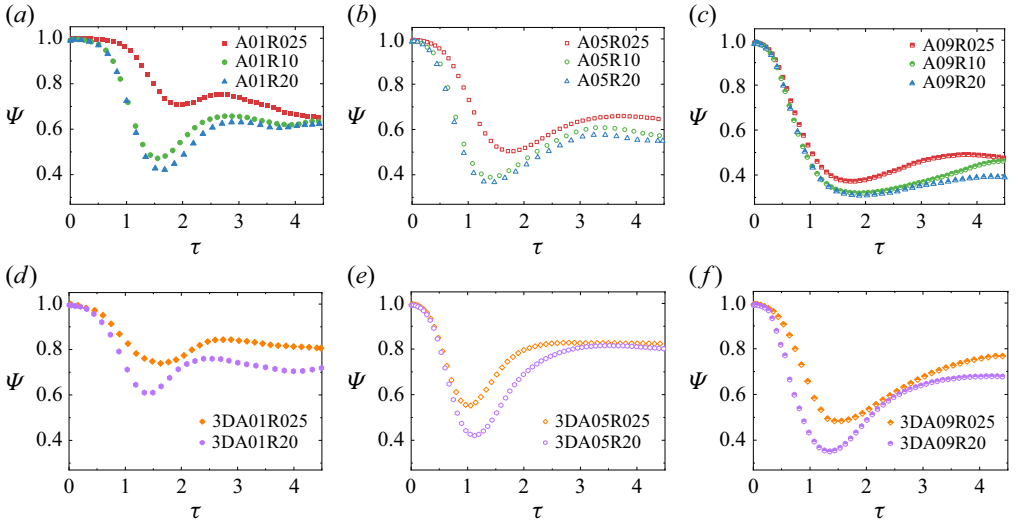


Figure 11. Temporal evolutions of the normalised mixed mass Ψ.

in rotation-driven RT turbulence, taking into account the unique mechanisms involved, such as the contribution of the Coriolis force.

The normalised mixed mass, which characterises the degree of fluid mixing, is another fundamental measurement of the evolution of the mixing layer, and is defined as (Zhou *et al.* 2016)

$$\Psi = \frac{\int \rho Y_h Y_l \, \mathrm{d}V}{\int \langle\rho\rangle\langle Y_h\rangle\langle Y_l\rangle \, \mathrm{d}V}. \tag{3.3}$$

Obviously, Ψ ranges from 0 to 1, corresponding to the completely segregated fluids to the completely mixed fluids. It is shown in figure 11 that the normalised mixed mass curves have valley values at early times, which is consistent with the observation in planar RT turbulence induced by a constant external acceleration g. Figure 11 shows that the value of Ψ at the same A_t decreases with increasing Ro, indicating that strong rotation is not

https://doi.org/10.1017/jfm.2025.10541 Published online by Cambridge University Press

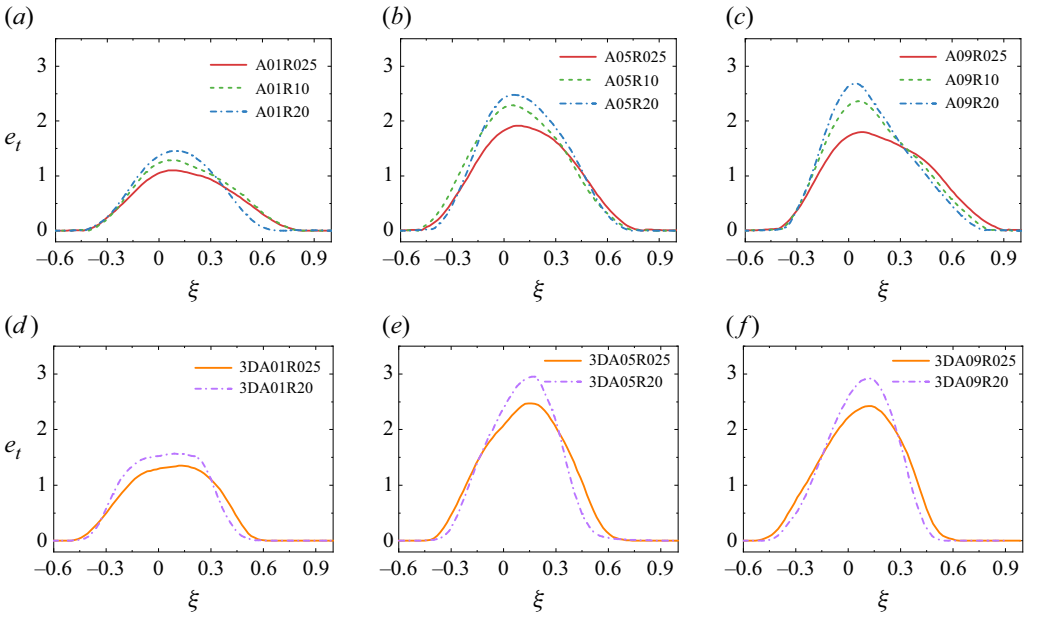


Figure 12. The radial distribution of e_t, defined as the turbulent kinetic energy $\langle \rho u_i'' u_i''/2 \rangle$ normalised by $[\rho u_i u_i/2]$, along the similarity variable ξ at $\tau = 4.5$.

conducive to overall fluid mixing within the mixing layer. Furthermore, for the same A_t and Ro, the normalised mixed mass of 3-D cases is greater than that of 2-D cases. This observation may be due to the stretching and tilting of the vortex structure in 3-D cases, which promotes fluid mixing. It should be noted that $\Psi = 1$ at the beginning is a result of initial mixing layer settings. This phenomenon, where $\Psi = 1$ at the beginning, is also observed in the study of RT flow (Zhou *et al.* 2016).

The above findings indicate that at the same A_t, rotation promotes the generation of small-scale structures but is detrimental to the overall mixing of fluids within the mixing layer. To provide an in-depth explanation of this phenomenon, the radial distributions of e_t and ψ are presented in figures 12 and 13, respectively. Here, e_t and ψ are defined as

$$e_t = \frac{\langle \rho u_i'' u_i''/2 \rangle}{[\rho u_i u_i/2]}, \quad \psi = \frac{\langle \rho Y_h Y_l \rangle}{[\langle \rho \rangle \langle Y_h \rangle \langle Y_l \rangle]}, \tag{3.4}$$

respectively. Indeed, e_t represents the turbulent kinetic energy $\langle \rho u_i'' u_i''/2 \rangle$ normalised by $[\rho u_i u_i/2]$, reflecting the generation of small-scale structures at the radial position r, and ψ is the mixed mass $\langle \rho Y_h Y_l \rangle$ normalised by $[\langle \rho \rangle \langle Y_h \rangle \langle Y_l \rangle]$, indicating the degree of mixing at the radial position r. It is important to clarify that we apply a Savitzky–Golay filter function with polynomial order 1 and window size 20 to the distributions of e_t and ψ in 2-D cases, as specified in Lavacot *et al.* (2024). This approach helps to mitigate the influence of limited statistical samples available in 2-D RT turbulence on the characteristics of physical quantity distributions (Lavacot *et al.* 2024).

As shown in figures 12 and 13, higher e_t correlates with greater ψ, indicating that fine-scale structures promote small-scale mixing. However, as Ro increases, e_t becomes more concentrated in the central region of the mixing layer, resulting in a sharper distribution curve. Consequently, as the rotation increases, ψ in the regions near the frontiers of the mixing layer is significantly reduced, resulting in an overall decrease in fluid mixing within the layer. Additionally, it is noteworthy that the distributions of e_t and ψ exhibit

https://doi.org/10.1017/jfm.2025.10541 Published online by Cambridge University Press

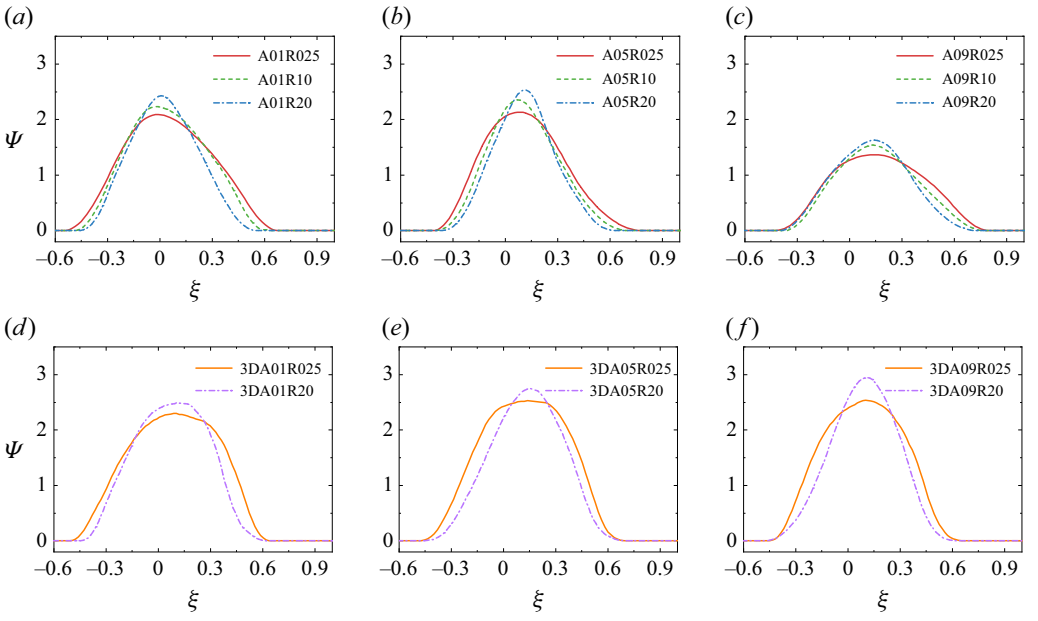


Figure 13. The radial distribution of ψ, defined as the mixed mass $\langle \rho Y_h Y_l \rangle$ normalised by $[\langle \rho \rangle \langle Y_h \rangle \langle Y_l \rangle]$, along the similarity variable ξ at $\tau = 4.5$.

asymmetry relative to the initial interface in figures 12 and 13, which stems from the asymmetries in flow evolution and cylindrical geometry. On the one hand, it is widely recognised that the evolution of bubble and spike mixing regions in RT turbulence is asymmetric, resulting in an asymmetric distribution of physical quantities relative to the initial interface (Zhou *et al.* 2016; Zhou 2017*b*). On the other hand, the cylindrical geometry and centrifugal force varying in the radial direction are inherently asymmetric with respect to the initial interface, leading to an asymmetric distribution of physical quantities. Thus the distributions of e_t and ψ are reasonably asymmetric due to the combined effects of asymmetries in flow evolution and cylindrical geometry.

3.4. *Theoretical model of the mixing layer growth*

Building on the approach employed by Zhao *et al.* (2021) in cylindrical RT turbulence without rotation, a theoretical model is proposed in this subsection to predict the growth of mixing width in rotation-driven RT turbulence with the initial perturbed interface r_0 and angular speed of rotating system Ω. Here, choosing the angular speed Ω to establish the model instead of Ro is for the convenience of model application. In this manner, other studies of rotation-driven RT turbulence can directly utilise the model without employing the present non-dimensionalisation approach. Since the mixing regions on both sides of the initial perturbed interface r_0 are asymmetrical, the inward and outward mixing layer widths, h_{in} and h_{out}, need to be modelled separately. Before establishing the model, it is essential to understand the physical mechanisms underlying the development of the mixing layer in RT turbulence. The basic mechanism of RT turbulence is the buoyancy-induced mixing of fluids (Boffetta & Mazzino 2017). For planar RT turbulence with a constant external acceleration g, the growth of the mixing width can be modelled by (Cook *et al.* 2004; Zhao *et al.* 2021)

$$\frac{\mathrm{d}\dot{h}_i}{\mathrm{d}t} = 2\alpha_i A_t g, \tag{3.5}$$

https://doi.org/10.1017/jfm.2025.10541 Published online by Cambridge University Press

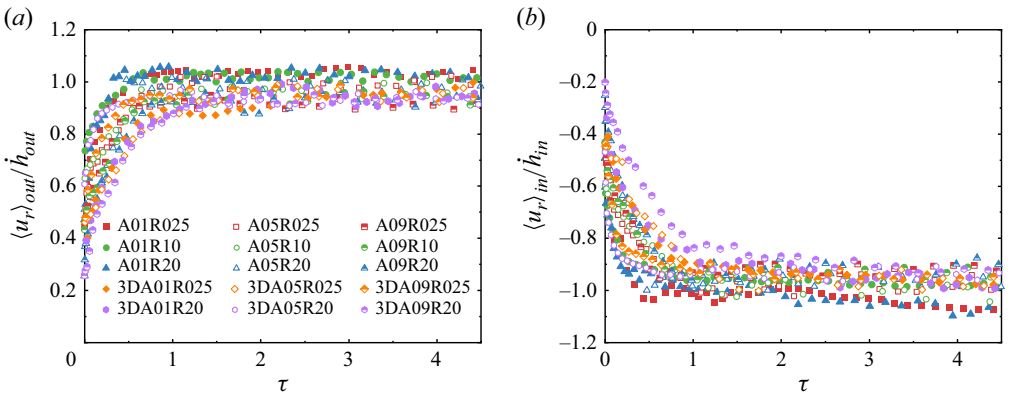


Figure 14. Ratios of the mean radial velocity at the positions of the (*a*) outer and (*b*) inner frontiers of the mixing layer to the growth velocity of the mixing layer versus the rescaled time τ.

where $i = b, s, h_b$ denotes the bubble mixing width, h_s represents the spike mixing width, and α_i denotes the dimensionless coefficient. In rotation-driven RT turbulence, the inward and outward mixing layers correspond to the bubble and spike regions, respectively. The flow mechanism described by (3.5) can be outlined as follows. The growth of the bubble and spike regions can be attributed to the buoyancy force expressed by A_t (denoting the density difference) and the external acceleration g. Specifically, the right-hand-side term denotes the average buoyancy force acting on the fluid parcels at the frontier of the mixing layer, and the left-hand-side term represents the acceleration of the mixing region, which can also be referred to as the acceleration of fluid parcels at the frontier of the mixing layer.

As for rotation-driven RT turbulence, the growth of bubbles and spikes in the corresponding pure fluids can also be viewed as result of the forces acting on the fluid parcels at the frontier of the mixing layer. Inspired by previous work (Zhao *et al.* 2021), the model for rotation-driven RT turbulence can be established by analysing the acceleration of the fluid parcels at the frontier of the mixing layer, and the forces acting on them. We first need to clarify the relationship between the growth speed of the mixing layer with the radial velocity of fluid parcels at the mixing frontiers. The ratios $\langle u_r \rangle_{in}/\dot{h}_{in}$ and $\langle u_r \rangle_{out}/\dot{h}_{out}$ at the inner and outer frontiers of the mixing layer, respectively, are presented in figure 14. Evidently, the absolute values of ratios remain within a narrow range 0.9–1.1 at $\tau \gtrsim 1.5$ when the flows reach turbulent states, indicating that the interface speed can be approximated by the mean radial velocity of parcels at mixing frontiers. Therefore, based on this approximation, the interface speed can be modelled by establishing the evolution equation for the radial velocity of fluid parcels at mixing frontiers using Newton's second law. The buoyancy force driving the parcels at the mixing frontiers in rotation-driven RT turbulence is caused by the centrifugal force and can be modelled in a form similar to (3.5), i.e. $2\alpha_i A_t \Omega^2 r_i$, where $i = out, in$. It is worth noting that the centrifugal force varies linearly along r, thus the modelled buoyancy force is related to the position of the frontier of the mixing layer r_i. However, in addition to the buoyancy force, the contribution of the Coriolis force in rotation-driven RT turbulence to the growth of the mixing layer must also be taken into account. The radial component of Coriolis force acting on fluid parcels can be formulated as the term $2\Omega u_\theta$. In order to quantitatively assess the contribution of the Coriolis force to the growth of the mixing layer, the ratios $\langle u_\theta \rangle_{in}/\dot{h}_{in}$ and $\langle u_\theta \rangle_{out}/\dot{h}_{out}$ at the inner and outer frontiers of the mixing layer, respectively, are plotted in figure 15. Evidently, the absolute values of ratios $\langle u_\theta \rangle_{out}/\dot{h}_{out}$ and $\langle u_\theta \rangle_{in}/\dot{h}_{in}$ remain within a

https://doi.org/10.1017/jfm.2025.10541 Published online by Cambridge University Press

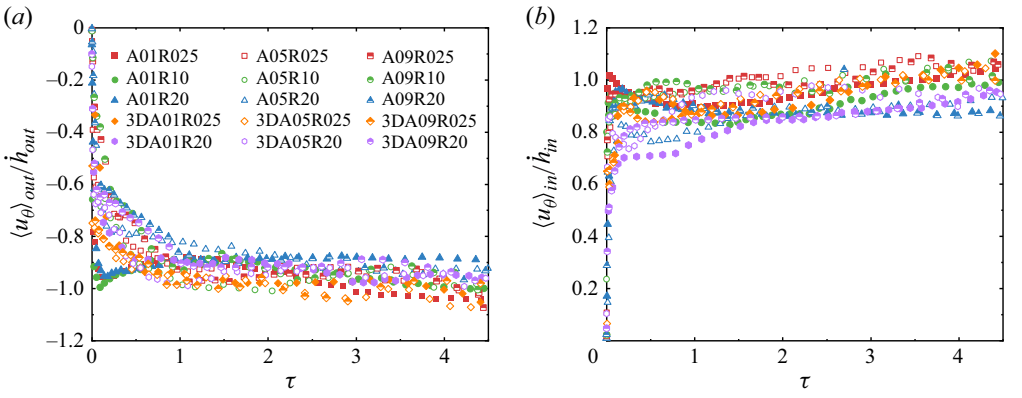


Figure 15. Ratios of the mean circumferential velocity at the positions of the (*a*) outer and (*b*) inner frontiers of the mixing layer to the growth speed of the mixing layer versus the rescaled time τ.

narrow range 0.85–1.1 at $\tau \gtrsim 1.5$ when the flows reach turbulent states. Therefore, it is reasonable to assume that the magnitudes of $\langle u_\theta \rangle$ at the inner and outer frontiers of the mixing layer are approximately equal to $\dot{h}_{in}$ and $\dot{h}_{out}$ during the turbulent mixing phase. Moreover, the ratios exhibit positive values at the inner mixing frontier, and negative values at the outer mixing frontier, indicating that $\langle u_\theta \rangle$ has different directions along the radial direction. To this end, the direction of the Coriolis force needs further determination, and the distributions of $\langle u_\theta \rangle$ at four different moments for four representative cases have been incorporated here. As shown in figure 16, the distributions of $\langle u_\theta \rangle$ show positive values in the inward mixing region, and negative values in the outward mixing region, indicating that the Coriolis force suppresses both the inward growth of the bubble region and the outward growth of the spike region. Hence the contribution of Coriolis force to the growth of the mixing layer in rotation-driven RT turbulence can be modelled as the term $-2\Omega\dot{h}_i$. It is clear that the forces in rotation-driven RT turbulence are more complex than those in cylindrical RT turbulence without rotation (Zhao *et al.* 2021). This is due to rotation, which causes buoyancy to be inhomogeneous along the radial direction, and introduces the Coriolis force.

In addition to the dynamic factors (i.e. the buoyancy force and Coriolis force), the average acceleration of fluid parcels at the mixing frontiers also needs to be determined. The radial acceleration a_r of each fluid parcel at the frontiers of the mixing layer in the cylindrical coordinate system is defined as

$$a_r = \frac{\mathrm{d}u_r}{\mathrm{d}t} - \frac{u_\theta^2}{r}. \tag{3.6}$$

Note that the average radial velocity $\langle u_r \rangle$ at the outer and inner frontiers of the mixing layer can be approximated as $\dot{h}_{out}$ and $-\dot{h}_{in}$, respectively, based on the results shown in figure 14. Moreover, the term u_θ^2/r describes the contribution of circumferential motion to the radial acceleration of the fluid parcel. As shown in figure 15, $\langle u_\theta \rangle$ values at the positions of the inner and outer frontiers of the mixing layer have the same order of magnitude as $\dot{h}_{in}$ and $\dot{h}_{out}$ when the flows reach the turbulent state. Therefore, the average term u_θ^2/r can be estimated as $\dot{h}_{out}^2/r_{out}$ and $\dot{h}_{in}^2/r_{in}$ for outward and inward mixing layers, respectively. Evidently, the acceleration in rotation-driven RT turbulence has the same form as that in cylindrical RT turbulence (Zhao *et al.* 2021), due to both occurring within cylindrical geometry. Given that the motions of fluid parcels are driven by buoyancy force and Coriolis

https://doi.org/10.1017/jfm.2025.10541 Published online by Cambridge University Press

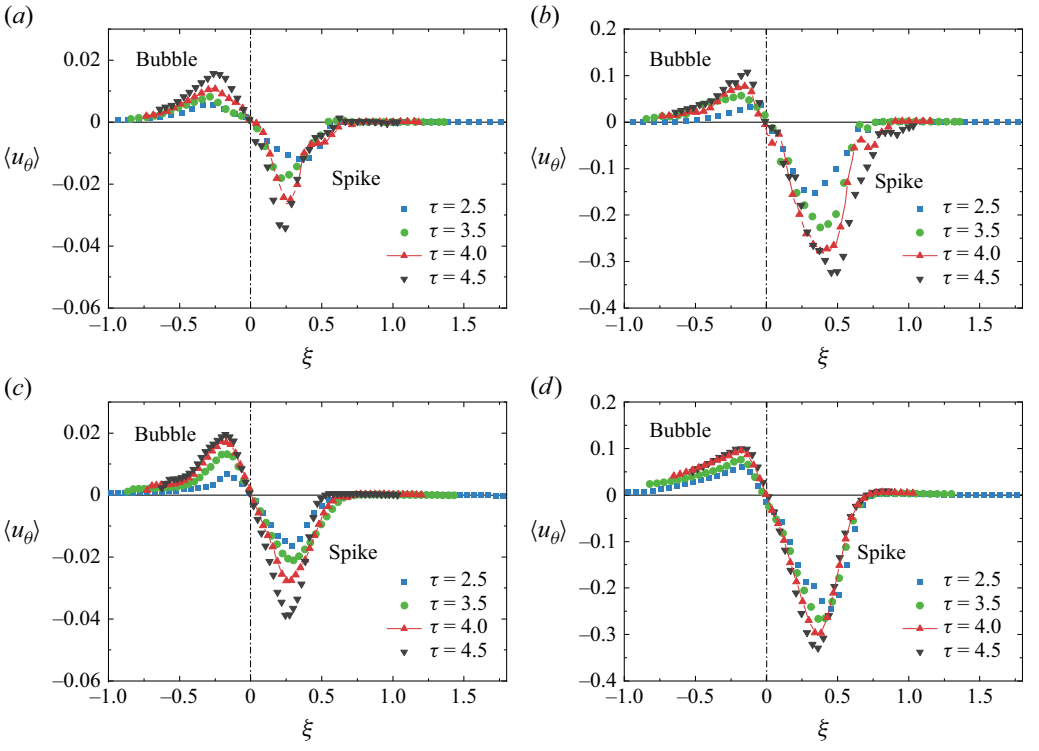


Figure 16. The distribution of the mean circumferential component of velocity u_θ at four different moments versus the similarity variable ξ for cases (*a*) A01R025, (*b*) A09R20, (*c*) 3DA01R025 and (*d*) 3DA01R20.

force, the model equations for the inward and outward mixing layers in rotation-driven RT turbulence can be derived in sequence as

$$\frac{\mathrm{d}\dot{h}_{out}}{\mathrm{d}t} - \frac{\dot{h}_{out}^2}{r_0 + h_{out}} = 2\alpha_{out} A_t \Omega^2 (r_0 + h_{out}) - 2\Omega \dot{h}_{out}, \tag{3.7}$$

$$\frac{\mathrm{d}\dot{h}_{in}}{\mathrm{d}t} + \frac{\dot{h}_{in}^2}{r_0 - h_{in}} = 2\alpha_{in} A_t \Omega^2 (r_0 - h_{in}) - 2\Omega \dot{h}_{in}. \tag{3.8}$$

To obtain the analytical expression of the mixing widths, (3.7) and (3.8) are divided by $r_0 + h_{out}$ and $r_0 - h_{in}$, respectively, allowing the left-hand sides of these equations to be formulated as

$$\frac{1}{r_0 + h_{out}} \frac{\mathrm{d}\dot{h}_{out}}{\mathrm{d}t} - \frac{\dot{h}_{out}^2}{(r_0 + h_{out})^2} = \frac{\mathrm{d}}{\mathrm{d}t}\left(\frac{\dot{h}_{out}}{r_0 + h_{out}}\right), \tag{3.9}$$

$$\frac{1}{r_0 - h_{in}} \frac{\mathrm{d}\dot{h}_{in}}{\mathrm{d}t} + \frac{\dot{h}_{in}^2}{(r_0 - h_{in})^2} = \frac{\mathrm{d}}{\mathrm{d}t}\left(\frac{\dot{h}_{in}}{r_0 - h_{in}}\right). \tag{3.10}$$

Therefore, after dividing (3.7) and (3.8) by $r_0 + h_{out}$ and $r_0 - h_{in}$, respectively, these equations can be further formulated as

$$\frac{\mathrm{d}}{\mathrm{d}t}\left(\frac{\dot{h}_{out}}{r_0 + h_{out}}\right) = 2\alpha_{out} A_t \Omega^2 - 2\Omega \frac{\dot{h}_{out}}{r_0 + h_{out}} \tag{3.11}$$

https://doi.org/10.1017/jfm.2025.10541 Published online by Cambridge University Press

and

$$\frac{\mathrm{d}}{\mathrm{d}t}\left(\frac{\dot{h}_{in}}{r_0 - h_{in}}\right) = 2\alpha_{in}A_t\Omega^2 - 2\Omega\frac{\dot{h}_{in}}{r_0 - h_{in}}, \tag{3.12}$$

respectively. Considering the initial mixing velocities $\dot{h}_{out}(0) = 0$ and $\dot{h}_{in}(0) = 0$, and then integrating the above equations over $\dot{h}_{out}/(r_0 + h_{out})$ and $\dot{h}_{in}/(r_0 - h_{in})$, gives

$$\frac{\dot{h}_{out}}{r_0 + h_{out}} = \alpha_{out}A_t\Omega(1 - \mathrm{e}^{-2\Omega t}) \tag{3.13}$$

and

$$\frac{\dot{h}_{in}}{r_0 - h_{in}} = \alpha_{in}A_t\Omega(1 - \mathrm{e}^{-2\Omega t}), \tag{3.14}$$

respectively. Finally, since the initial mixing widths are zero, the widths of the outward and inward mixing layers can be obtained by integrating (3.13) and (3.14), respectively, i.e.

$$\frac{h_{out}}{r_0} = \exp\left[\frac{1}{2}\alpha_{out}A_t\left(\mathrm{e}^{-2\Omega t} + 2\Omega t - 1\right)\right] - 1 \tag{3.15}$$

and

$$\frac{h_{in}}{r_0} = 1 - \exp\left[-\frac{1}{2}\alpha_{in}A_t\left(\mathrm{e}^{-2\Omega t} + 2\Omega t - 1\right)\right]. \tag{3.16}$$

Based on the theoretical model of mixing width, the rescaled time $\tau = A_t(\mathrm{e}^{-2\Omega t} + 2\Omega t - 1)$ is a natural choice to describe the evolution of the mixing layer in rotation-driven RT turbulence with various A_t and Ω.

Despite the theoretical relations (3.15) and (3.16) having been derived, the dimensionless coefficients α_{out} and α_{in} still need to be determined to obtain usable models. In previous studies on planar RT turbulence, these coefficients are calculated using quantities related to mixing velocities and widths (Cook & Dimotakis 2001; Cabot & Cook 2006), i.e. $\alpha_i = \dot{h}^2/4A_tgh$. In a similar manner, the dimensionless coefficients for rotation-driven RT turbulence can be obtained based on (3.13) and (3.14) as

$$\alpha_{out} = \frac{\dot{h}_{out}(t)}{r_0 + h_{out}(t)}\frac{1}{A_t\Omega(1 - \mathrm{e}^{-2\Omega t})} \tag{3.17}$$

and

$$\alpha_{in} = \frac{\dot{h}_{in}(t)}{r_0 - h_{in}(t)}\frac{1}{A_t\Omega(1 - \mathrm{e}^{-2\Omega t})}, \tag{3.18}$$

respectively, which yield corresponding results shown in figure 17. It is evident that α_{out} and α_{in} tend to reach a quasi-steady value at $\tau \gtrsim 1$ for all cases listed in table 2. Therefore, both dimensionless coefficients α_{out} and α_{in} are approximately 0.3 for rotation-driven RT turbulence.

To verify the accuracy of the theoretical models (3.15) and (3.16), the positions of the outward (i.e. $r_{out} = r_0 + h_{out}$) and inward (i.e. $r_{in} = r_0 - h_{in}$) frontiers of the mixing layer calculated by the models are compared with those obtained from the DNS results. As depicted in figure 18, the excellent agreement between the models and DNS results confirms that the current models (3.15) and (3.16) can be reliably used to predict the growth of the mixing layer in rotation-driven RT turbulence. Furthermore, the symbols of all cases

https://doi.org/10.1017/jfm.2025.10541 Published online by Cambridge University Press

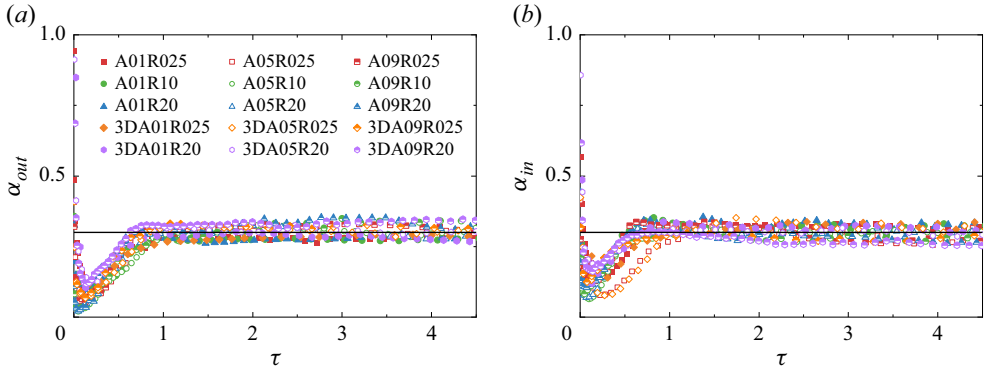


Figure 17. The dimensionless coefficients (*a*) α_{out} and (*b*) α_{in} in the theoretical models of mixing widths in rotation-driven RT turbulence.

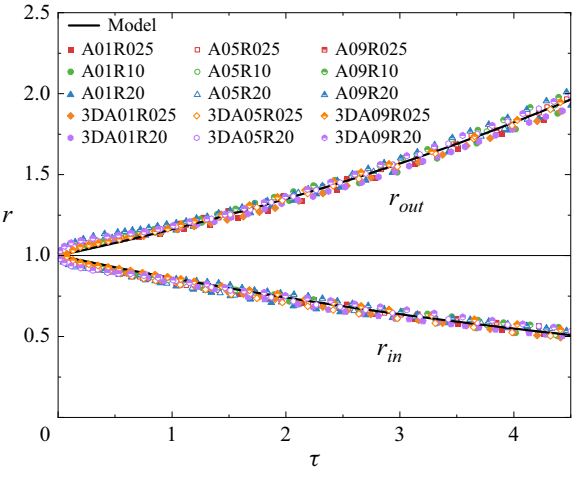


Figure 18. The positions of the outer and inner frontiers of the mixing layer in rotation-driven RT turbulence. Here, the lines represent the results of theoretical models, while the symbols denote the results of DNS.

collapse together well, indicating that the evolution of the mixing layer in rotation-driven RT turbulence can be unified based on the rescaled time τ.

It can be confirmed that the current models for rotation-driven RT turbulence can be reduced to quadratic growth for planar RT turbulence induced by constant external acceleration. To this end, the Taylor expansions of growth laws of mixing layers (3.15) and (3.16) are

$$h_{out} = \alpha_{out} A_t \Omega^2 r_0 t^2 - \frac{2}{3}\alpha_{out} A_t \Omega^3 r_0 t^3 + \left(\frac{1}{2}\alpha_{out}^2 A_t^2 + \frac{1}{3}\alpha_{out} A_t\right) \Omega^4 r_0 t^4 + \cdots \quad (3.19)$$

and

$$h_{in} = \alpha_{in} A_t \Omega^2 r_0 t^2 - \frac{2}{3}\alpha_{in} A_t \Omega^3 r_0 t^3 - \left(\frac{1}{2}\alpha_{in}^2 A_t^2 - \frac{1}{3}\alpha_{in} A_t\right) \Omega^4 r_0 t^4 + \cdots , \quad (3.20)$$

respectively. Moreover, the growth features of the mixing layer in rotation-driven RT turbulence manifest in the effects of geometrical curvature (i.e. $1/r_0$) and radial inhomogeneity of the centrifugal force (i.e. $\Omega^2(r_0 \pm h_i)$, where $+$ is for h_{out}, and $-$ is

https://doi.org/10.1017/jfm.2025.10541 Published online by Cambridge University Press

for h_{in}) inducing the instability and Coriolis force ($\Omega\dot{h}_i$). However, these effects can be eliminated by taking limits with Ω and r_0 at a fixed A_t and a given time t. Specifically, the effects of cylindrical geometry, governed by $1/r_0$, becomes negligible as $r_0 \to \infty$. The effects of radial inhomogeneity of the centrifugal force, characterised by $\Omega^2(r_0 \pm h_i)$, and of the Coriolis force, determined by $2\Omega\dot{h}_i$, can be neglected as $\Omega \to 0$. It is worth noting that Ω and r_0 should also satisfy the condition $\Omega^2 r_0 \to g$ with a constant g to ensure the driving instability. As a result, the third- and higher-degree terms in the Taylor expansions (3.19) and (3.20) become infinitesimal at any given moment t and fixed A_t since $\Omega^m r_0 \to 0$ for $m \geqslant 3$. Overall, (3.19) and (3.20) can be reduced as $h_{out} = \alpha_{out} A_t g t^2$ and $h_{in} = \alpha_{in} A_t g t^2$. The reduced formulation of the mixing width is exactly the same as that in planar RT turbulence induced by constant external acceleration (Cook *et al.* 2004; Ristorcelli & Clark 2004; Zhao *et al.* 2020*a*). This analysis further mathematically confirms the reliability of the current theoretical models of mixing widths in rotation-driven RT turbulence.

Although the establishment of the model for rotation-driven RT turbulence follows the same approach as that for cylindrical RT turbulence (Zhao *et al.* 2021), their fundamentally different driving mechanisms preclude a direct reduction of the former model to the latter case. Indeed, there is a significant difference in the evolution of the mixing layer between the cylindrical RT turbulence and the rotation-driven RT turbulence, despite both cases sharing a similar flow configuration. It originates in the different driving mechanisms: cylindrical RT turbulence is driven by a constant external acceleration g, whereas rotation-driven RT turbulence considered here is driven by rotation. Essentially, the evolution of the mixing layer in rotation-driven RT turbulence is governed by the combined effects of geometric curvature, the Coriolis force, and the radial inhomogeneity of the centrifugal force. Due to the fact that geometric curvature is nonlinearly coupled with the Coriolis force and the radial inhomogeneity of the centrifugal force, it is impossible to isolate the effect of geometric curvature while ignoring the other two factors. Specifically, as $\Omega \to 0$, the influences of the Coriolis force and the radial inhomogeneity of the centrifugal force become negligible. Meanwhile, to maintain the driving instability, Ω and r_0 must satisfy the condition $\Omega^2 r_0 \to g$ with a constant g. This implies that $r_0 \sim \Omega^{-2} \to \infty$, resulting in the geometric curvature's impact becoming negligible in this regime. Therefore, neither factor can be disregarded independently, preventing a direct reduction of the centrifugal RT turbulence model to the cylindrical RT turbulence model (Zhao *et al.* 2021).

4. Conclusions

In this paper, we have conducted numerical and theoretical investigations on the evolution of the mixing layer in rotation-driven RT turbulence. The flow features of the mixing layer are initially examined via DNS results. It is found that the mixing layer in rotation-driven RT turbulence covers a wide range of length scales. The strong rotation in rotation-driven RT turbulence at the same A_t enhances the generation of fine-scale structures that promote the small-scale mixing, yet it does not promote overall fluid mixing within the mixing layer. It is further revealed that the evolution of the mixing layer in rotation-driven RT turbulence exhibits self-similarity, but the growth of the mixing layer does not conform to the quadratic growth observed in planar RT turbulence induced by constant external acceleration. To address this, a theoretical model for predicting the mixing widths of rotation-driven RT turbulence is developed based on the approach utilised in cylindrical RT turbulence without rotation (Zhao *et al.* 2021), and this is validated using DNS results. Furthermore, utilising the theoretical model of mixing widths, the rescaled time $\tau = A_t(\mathrm{e}^{-2\Omega t} + 2\Omega t - 1)$ is formulated to unify the evolution of the mixing layer in

https://doi.org/10.1017/jfm.2025.10541 Published online by Cambridge University Press

rotation-driven RT turbulence with various values of A_t and Ro. Finally, it is identified that the growth laws for rotation-driven RT turbulence can be reduced to quadratic growth when the effects of geometrical curvature, radial inhomogeneity of the centrifugal force, and Coriolis force become negligible. This analysis further substantiates the validity of the current theoretical models of mixing widths for rotation-driven RT turbulence mathematically.

Acknowledgements. The authors are very grateful to Dr Y.-S. Zhang at the Institute of Applied Physics and Computational Mathematics for useful discussions on the algorithm and code.

Funding. This work was supported by the National Natural Science Foundation of China (nos 12202436, 12388101), by the Science Challenge Project, by the LCP Fund for Young Scholars (no. 6142A05QN22002), and by the Strategic Priority Research Programme of the Chinese Academy of Sciences (no. XDB0500301).

Declaration of interests. The authors report no conflict of interest.

References

Abarzhi, S.I. & Sreenivasan, K.R. 2022 Self-similar Rayleigh–Taylor mixing with accelerations varying in time and space. *Proc. Natl Acad. Sci. USA* **119** (47), e2118589119.

Akula, B., Suchandra, P., Mikhaeil, M. & Ranjan, D. 2017 Dynamics of unstably stratified free shear flows: an experimental investigation of coupled Kelvin–Helmholtz and Rayleigh–Taylor instability. *J. Fluid Mech.* **816**, 619–660.

Andrews, M.J. & Spalding, D.B. 1990 A simple experiment to investigate two-dimensional mixing by Rayleigh–Taylor instability. *Phys. Fluids A* **2** (6), 922–927.

Baldwin, K.A., Scase, M.M. & Hill, R.J.A. 2015 The inhibition of the Rayleigh–Taylor instability by rotation. *Sci. Rep.* **5**, 11706.

Bodner, S.E. 1974 Rayleigh–Taylor instability and laser-pellet fusion. *Phys. Rev. Lett.* **33**, 761–764.

Boffetta, G. & Mazzino, A. 2017 Incompressible Rayleigh–Taylor turbulence. *Annu. Rev. Fluid Mech.* **49**, 119–143.

Boffetta, G., Mazzino, A. & Musacchio, S. 2016 Rotating Rayleigh–Taylor turbulence. *Phys. Rev. Fluids* **1**, 054405.

Buyko, A.M., Garanin, S.F., Mokhov, V.N. & Yakubov, V.B. 1997 Possibility of low-dense magnetized DT plasma ignition threshold achievement in a MAGO system. *Laser Part. Beams* **15** (1), 127–132.

Cabot, W. & Zhou, Y. 2013 Statistical measurements of scaling and anisotropy of turbulent flows induced by Rayleigh–Taylor instability. *Phys. Fluids* **25** (1), 015107.

Cabot, W.H. & Cook, A.W. 2006 Reynolds number effects on Rayleigh–Taylor instability with possible implications for type Ia supernovae. *Nat. Phys.* **2** (8), 562–568.

Caproni, A., Lanfranchi, G.A., da Silva, A.L. & Falceta-Gonçalves, D. 2015 Three-dimensional hydrodynamical simulations of the supernovae-driven gas loss in the dwarf spheroidal galaxy Ursa Minor. *Astrophys. J.* **805**, 109.

Carnevale, G.F., Orlandi, P., Zhou, Y. & Kloosterziel, R.C. 2002 Rotational suppression of Rayleigh–Taylor instability. *J. Fluid Mech.* **457**, 181–190.

Ceci, A. & Pirozzoli, S. 2025 Direct numerical simulation study of turbulent pipe flow with imposed radial rotation. *J. Fluid Mech.* **1004**, A15.

Cherfils, C. & Mikaelian, K.O. 1996 Simple model for the turbulent mixing width at an ablating surface. *Phys. Fluids* **8** (2), 522–535.

Cook, A.W., Cabot, W. & Miller, P.L. 2004 The mixing transition in Rayleigh–Taylor instability. *J. Fluid Mech.* **511**, 333–362.

Cook, A.W. & Dimotakis, P.E. 2001 Transition stages of Rayleigh–Taylor instability between miscible fluids. *J. Fluid Mech.* **443**, 69–99.

Cook, A.W. & Zhou, Y. 2002 Energy transfer in Rayleigh–Taylor instability. *Phys. Rev. E* **66** (2), 026312.

Cui, A.Q. & Street, R.L. 2004 Large-eddy simulation of coastal upwelling flow. *Environ. Fluid Mech.* **4**, 197–223.

Dimonte, G. 2000 Spanwise homogeneous buoyancy-drag model for Rayleigh–Taylor mixing and experimental evaluation. *Phys. Plasmas* **7** (6), 2255–2269.

Dimotakis, P.E. 2000 The mixing transition in turbulent flows. *J. Fluid Mech.* **409**, 69–98.

https://doi.org/10.1017/jfm.2025.10541 Published online by Cambridge University Press

ECKE, R.E. & SHISHKINA, O. 2023 Turbulent rotating Rayleigh–Bénard convection. *Annu. Rev. Fluid Mech.* **55** (1), 603–638.

FU, C.-Q., ZHAO, Z., WANG, P., LIU, N.-S., WAN, Z.-H. & LU, X.-Y. 2023 Bubble re-acceleration behaviours in compressible Rayleigh–Taylor instability with isothermal stratification. *J. Fluid Mech.* **954**, A16.

FU, C.-Q., ZHAO, Z.-Y., XU, X., WANG, P., LIU, N.-S., WAN, Z.-H. & LU, X.-Y. 2022 Nonlinear saturation of bubble evolution in a two-dimensional single-mode stratified compressible Rayleigh–Taylor instability. *Phys. Rev. Fluids* **7** (2), 023902.

GAUTHIER, S. 2017 Compressible Rayleigh–Taylor turbulent mixing layer between Newtonian miscible fluids. *J. Fluid Mech.* **830**, 211–256.

GE, J., ZHANG, X.-T., LI, H.-F. & TIAN, B.-L. 2020 Late-time turbulent mixing induced by multimode Richtmyer–Meshkov instability in cylindrical geometry. *Phys. Fluids* **32** (12), 124116.

GELFAND, J.D., SLANE, P.O. & ZHANG, W.-Q. 2009 A dynamical model for the evolution of a pulsar wind nebula inside a nonradiative supernova remnant. *Astrophys. J.* **703**, 2051–2067.

GUO, H.-Y., YU, X.-J., WANG, L.-F., YE, W.-H., WU, J.-F. & LI, Y.-J. 2014 On the second harmonic generation through bell–Plesset effects in cylindrical geometry. *Chin. Phys. Lett.* **31** (4), 044702.

HILLIER, A. 2020 Self-similar solutions of asymmetric Rayleigh–Taylor mixing. *Phys. Fluids* **32** (1), 015103.

HINDS, W.C., ASHLEY, A., KENNEDY, N.J. & BUCKNAM, P. 2002 Conditions for cloud settling and Rayleigh–Taylor instability. *Aerosol Sci. Technol.* **36**, 1128–1138.

HU, R.-N., LI, X.-L. & YU, C.-P. 2024 Effects of streamwise rotation on helicity and vortex in channel turbulence. *J. Fluid Mech.* **980**, A50.

HUNEAULT, J., PLANT, D. & HIGGINS, A.J. 2019 Rotational stabilisation of the Rayleigh–Taylor instability at the inner surface of an imploding liquid shell. *J. Fluid Mech.* **873**, 531–567.

JIANG, H.-C., WANG, D.-P., LIU, S. & SUN, C. 2022 Experimental evidence for the existence of the ultimate regime in rapidly rotating turbulent thermal convection. *Phys. Rev. Lett.* **129** (20), 204502.

JIANG, H.-C., ZHU, X.-J., WANG, D.-P., HUISMAN, S.G. & SUN, C. 2020 Supergravitational turbulent thermal convection. *Sci. Adv.* **6** (40), eabb8676.

KORD, A. & CAPECELATRO, J. 2019 Optimal perturbations for controlling the growth of a Rayleigh–Taylor instability. *J. Fluid Mech.* **876**, 150–185.

LAVACOT, D.-L., LIU, J., WILLIAMS, H., MORGAN, B.E. & MANI, A. 2024 Non-locality of mean scalar transport in two-dimensional Rayleigh–Taylor instability using the macroscopic forcing method. *J. Fluid Mech.* **985**, A47.

LIU, W.-H., YU, C.-P., YE, W.-H. & WANG, L.-F. 2014 Nonlinear saturation amplitude of cylindrical Rayleigh–Taylor instability. *Chin. Phys. B* **23** (9), 094502.

LIVESCU, D. 2013 Numerical simulations of two-fluid turbulent mixing at large density ratios and applications to the Rayleigh–Taylor instability. *Phil. Trans R. Soc. Lond. A*, **371**(2003), 20120185.

LIVESCU, D., WEI, T. & BRADY, P.T. 2021 Rayleigh–Taylor instability with gravity reversal. *Physica D* **417**, 132832.

LUO, T.-F. & WANG, J.-C. 2021 Effects of Atwood number and stratification parameter on compressible multi-mode Rayleigh–Taylor instability. *Phys. Fluids* **33**, 115111.

OLSON, D.H. & JACOBS, J.W. 2009 Experimental study of Rayleigh–Taylor instability with a complex initial perturbation. *Phys. Fluids* **21** (3), 034103.

RAYLEIGH, L. 1882 Investigation of the character of the equilibrium of an incompressible heavy fluid of variable density. *Proc. R. Math. Soc.* **s1-14**, 170–177.

READ, K.I. 1984 Experimental investigation of turbulent mixing by Rayleigh–Taylor instability. *Physica D* **12** (1–3), 45–58.

RECKINGER, S.J., LIVESCU, D. & VASILYEV, O.V. 2016 Comprehensive numerical methodology for direct numerical simulations of compressible Rayleigh–Taylor instability. *J. Comput. Phys.* **313**, 181–208.

RISTORCELLI, J.R. & CLARK, T.T. 2004 Rayleigh–Taylor turbulence: self-similar analysis and direct numerical simulations. *J. Fluid Mech.* **507**, 213–253.

SCASE, M.M., BALDWIN, K.A. & HILL, R.J.A. 2017 Rotating Rayleigh–Taylor instability. *Fluids* **2**, 024801.

SCASE, M.M., BALDWIN, K.A. & HILL, R.J.A. 2020 Magnetically induced Rayleigh–Taylor instability under rotation: comparison of experimental and theoretical results. *Phys. Rev. E* **102**, 043101.

SCASE, M.M. & HILL, R.J.A. 2018 Centrifugally forced Rayleigh–Taylor instability. *J. Fluid Mech.* **852**, 543–577.

SCASE, M.M. & SENGUPTA, S. 2021 Cylindrical rotating Rayleigh–Taylor instability. *J. Fluid Mech.* **907**, A33.

SCHULTZ, D.M., *et al.* 2006 The mysteries of mammatus clouds: observations and formation mechanisms. *J. Atmos. Sci.* **63**, 2409–2435.

https://doi.org/10.1017/jfm.2025.10541 Published online by Cambridge University Press

SUCHANDRA, P. & RANJAN, D. 2023 Dynamics of multilayer Rayleigh–Taylor instability at moderately high Atwood numbers. *J. Fluid Mech.* **974**, A35.

TAO, J.-J., HE, X.-T., YE, W.-H. & BUSSE, F.H. 2013 Nonlinear Rayleigh–Taylor instability of rotating inviscid fluids. *Phys. Rev. E* **87**, 013001.

TAYLOR, G.I. 1950 The instability of liquid surfaces when accelerated in a direction perpendicular to their planes. I. *Proc. R. Soc. Lond. A* **201**, 192–196.

TENG, H., LIU, N.-S., LU, X.-Y. & KHOMAMI, B. 2015 Direct numerical simulation of Taylor–Couette flow subjected to a radial temperature gradient. *Phys. Fluids* **27** (12), 125101.

TRITSCHLER, V.K., ZUBEL, M., HICKEL, S. & ADAMS, N.A. 2014 Evolution of length scales and statistics of Richtmyer–Meshkov instability from direct numerical simulations. *Phys. Rev. E* **90** (6), 063001.

WANG, L.-F., WU, J.-F., YE, W.-H., ZHANG, W.-Y. & HE, X.-T. 2013 Weakly nonlinear incompressible Rayleigh–Taylor instability growth at cylindrically convergent interfaces. *Phys. Plasmas* **20** (4), 042708.

WEI, Y.-K., LI, Y.-M., WANG, Z.-D., YANG, H., ZHU, Z.-C., QIAN, Y.-H. & LUO, K.-H. 2022 Small-scale fluctuation and scaling law of mixing in three-dimensional rotating turbulent Rayleigh–Taylor instability. *Phys. Rev. E* **105**, 015103.

WOOSLEY, S.E., WUNSCH, S. & KUHLEN, M. 2004 Carbon ignition in type Ia supernovae: an analytic model. *Astrophys. J.* **607** (2), 921.

YANG, Y.-L., WANG, C.-L., GUO, R. & ZHANG, M.-Q. 2023 Numerical analyses of the flow past a short rotating cylinder. *J. Fluid Mech.* **975**, A15.

YAO, Z.-Z., EMRAN, M.S., TEIMURAZOV, A. & SHISHKINA, O. 2025 Direct numerical simulations of centrifugal convection: from gravitational to centrifugal buoyancy dominance. *Intl J. Heat Mass Transfer* **236**, 126314.

YEUNG, P.-K. & POPE, S.B. 1989 Lagrangian statistics from direct numerical simulations of isotropic turbulence. *J. Fluid Mech.* **207**, 531–586.

YOUNGS, D.L. 1984 Numerical simulation of turbulent mixing by Rayleigh–Taylor instability. *Physica D* **12** (1), 32–44.

YOUNGS, D.L. 2013 The density ratio dependence of self-similar Rayleigh–Taylor mixing. *Phil. Trans R. Soc. Lond. A*, **371**(2003), 20120173.

YUAN, M., ZHAO, Z.-Y., LIU, L.-Q., WANG, P., LIU, N.-S. & LU, X.-Y. 2023 Instability evolution of a shock-accelerated thin heavy fluid layer in cylindrical geometry. *J. Fluid Mech.* **969**, A6.

ZHANG, H., BETTI, R., YAN, R. & ALUIE, H. 2020 Nonlinear bubble competition of the multimode ablative Rayleigh–Taylor instability and applications to inertial confinement fusion. *Phys. Plasmas* **27** (12), 122701.

ZHANG, Z.-P. & WANG, B.-C. 2024 Direct numerical simulation of turbulent flow and structures in a circular pipe subjected to axial system rotation. *J. Fluid Mech.* **1000**, A1.

ZHAO, D.-X., BETTI, R. & ALUIE, H. 2022 Scale interactions and anisotropy in Rayleigh–Taylor turbulence. *J. Fluid Mech.* **930**, A29.

ZHAO, Z.-Y., LIU, N.-S. & LU, X.-Y. 2020*a* Kinetic energy and enstrophy transfer in compressible Rayleigh–Taylor turbulence. *J. Fluid Mech.* **904**, A37.

ZHAO, Z.-Y., WANG, P., LIU, N.-S. & LU, X.-Y. 2020*b* Analytical model of nonlinear evolution of single-mode Rayleigh–Taylor instability in cylindrical geometry. *J. Fluid Mech.* **900**, A24.

ZHAO, Z.-Y., WANG, P., LIU, N.-S. & LU, X.-Y. 2021 Scaling law of mixing layer in cylindrical Rayleigh–Taylor turbulence. *Phys. Rev. E* **104** (5), 055104.

ZHONG, J., WANG, D.-P. & SUN, C. 2023 From sheared annular centrifugal Rayleigh–Bénard convection to radially heated Taylor–Couette flow: exploring the impact of buoyancy and shear on heat transfer and flow structure. *J. Fluid Mech.* **972**, A29.

ZHOU, Q. 2013 Temporal evolution and scaling of mixing in two-dimensional Rayleigh–Taylor turbulence. *Phys. Fluids* **25** (8), 085107.

ZHOU, Y. 2017*a* Rayleigh–Taylor and Richtmyer–Meshkov instability induced flow, turbulence, and mixing I. *Phys. Rep.* **720**, 1–136.

ZHOU, Y. 2017*b* Rayleigh–Taylor and Richtmyer–Meshkov instability induced flow, turbulence, and mixing II. *Phys. Rep.* **723**, 1–160.

ZHOU, Y., CABOT, W.H. & THORNBER, B. 2016 Asymptotic behavior of the mixed mass in Rayleigh–Taylor and Richtmyer–Meshkov instability induced flows. *Phys. Plasmas* **23** (5), 052712.

ZHU, Y.-B., SONG, J.-X., LIN, F.-H., LIU, N.-S., LU, X.-Y. & KHOMAMI, B. 2022 Relaminarization of spanwise-rotating viscoelastic plane Couette flow via a transition sequence from a drag-reduced inertial to a drag-enhanced elasto-inertial turbulent flow. *J. Fluid Mech.* **931**, R7.

https://doi.org/10.1017/jfm.2025.10541 Published online by Cambridge University Press